ELECTRONIC NOISE IN NANOSTRUCTURES:

LIMITATIONS AND SENSING APPLICATIONS

A Dissertation

by

JONG UN KIM

Submitted to the Office of Graduate Studies of
Texas A&M University
in partial fulfillment of the requirements for the degree of

DOCTOR OF PHILOSOPHY

December 2006

Major Subject: Electrical Engineering

ELECTRONIC NOISE IN NANOSTRUCTURES:

LIMITATIONS AND SENSING APPLICATIONS

A Dissertation

by

JONG UN KIM

Submitted to the Office of Graduate Studies of
Texas A&M University
in partial fulfillment of the requirements for the degree of

DOCTOR OF PHILOSOPHY

Approved by:

Chair of Committee,	Laszlo B. Kish
Committee Members,	Jun Kameoka
	Arum Han
	Ricardo Gutierrez-Osuna
Head of Department,	Costas N. Georghiades

December 2006

Major Subject: Electrical Engineering

ABSTRACT

Electronic Noise in Nanostructures:
Limitations and Sensing Applications. (December 2006)
Jong Un Kim, B.S.; M.S.; Ph.D.; Seoul National University;
M.S., Texas A&M University
Chair of Advisory Committee: Dr. Laszlo B. Kish

Nanostructures are nanometer scale structures (characteristic length less than 100 nm) such as nanowires, ultra-small junctions, etc. Since nanostructures are less stable, their characteristic volume is much smaller compared to defect sizes and their characteristic length is close to acoustical phonon wavelength. Moreover, because nanostructures include significantly fewer charge carriers than microscale structures, electronic noise in nanostructures is enhanced compared to microscale structures. Additionally, in microprocessors, due to the small gate capacitance and reduced noise margin (due to reduced supply voltage to keep the electrical field at a reasonable level), the electronic noise results in bit errors. On the other hand, the enhanced noise is useful for advanced sensing applications which are called fluctuation-enhanced sensing. In this dissertation, we first survey our earlier results about the limitation of noise posed on specific nano processors. Here, single electron logic is considered for voltage controlled logic with thermal excitations and generic shot noise is considered for current-controlled logic. Secondly, we discuss our recent results on the electronic noise in nanoscale sensors for SEnsing of Phage-Triggered Ion Cascade (SEPTIC, for instant bacterial detection) and for silicon nanowires for viral sensing. In the sensing of the phage-triggered ion cascade sensor, bacteriophage-infected bacteria release potassium ions and move randomly at the same time; therefore, electronic noise (i.e., stochastic signals) are generated. As an advanced model, the electrophoretic effect in the SEPTIC sensor is discussed. In the viral sensor, since the combination of the analyte and a specific receptor located at the surface of the silicon nanowire occurs randomly in space and time, a stochastic signal is obtained. A mathematical model for a pH silicon nanowire nanosensor is developed and the size quantization effect in the nanosensor is also discussed. The calculation results are in excellent agreement with the experimental results in the literature.

DEDICATION

To my wife, Rira

ACKNOWLEDGMENTS

I would like to thank my committee chair, Dr. Kish, and my committee members, Dr. Kameoka, Dr. Han, and Dr. Gutierrez-Osuna, for their guidance and support throughout the course of this research. I acknowledge that the nano-gap probes for our SEPTIC experiments were fabricated by the group of Dr. Mosong Cheng in the Electrical and Computer Engineering Department, the bacterium and phage solution were from the group of Dr. Ryland Young, and the test samples were prepared by Dr. Maria King at the Biochemistry/Biophysics Department; and I also appreciate their help.

TABLE OF CONTENTS

LIST OF FIGURES

LIST OF TABLES

CHAPTER I

INTRODUCTION

Nanotechnology is generally regarded as technology dealing with nanostructures whose characteristic size is between 1 and 100 nanometers (nm). Here, a nanometer is one billionth of a meter. There are several kinds of nanostructures such as quantum dots (QD), quantum wires, nanowires, ultrasmall junction, and carbon nanotubes and so on. Electronic band structures are modified in quantum dots and wires due to size quantization effect [1]. The size quantization effect makes the energy gap larger between the lowest conduction and the highest valence bands (or levels) and space-dependent density of state. From the electronic transport point of view, the size quantization effect results in two (or one)-dimensional transport. Another important electronic phenomenon at nanostructures is single electron tunneling; only a single electron can tunnel through an ultrasmall junction at a time [2]. A junction connected between a nanostructure and an electrode or nanostructures can be the ultrasmall junction, and the capacitance of the ultrasmall junction for the single electron tunneling has to be small enough for the electrostatic energy to be greater than thermal energy [3].

The characteristic length of nanostructures is approximately equal to the size of a set of hundreds of chemical molecules or of a single biological macromolecule such as a bacterial cell, DNA, and protein and so on. Moreover, when nanostructures on a substrate are submerged in a sample solution, only a single bacterium or virus can affect the surface of the nanostructures [4]. Therefore, the sensitivity of nanoscale sensors, so called nanosensors, is enhanced so incredibly that nanosensors can detect a single biomolecule behavior [4,5].

There are two approaches to fabricate nanostructures: *top-down* and *bottom-up* [6]. The conventional semiconductor processes are used in the top-down approach, while self-assembly, colloidal chemistry, and vapor-liquid-solid techniques are used in the bottom-up approach. There are many methods to synthesize nanostructures, especially quantum dots in the bottom-up approach, e.g., chemical reactions in colloidal solutions, long time annealing in solid state, chemical vapor deposition on solid surface, and wet or dry etching of thin film on solid surface, and so on. The bottom-up approach provides relatively economical and convenient synthesis of nanostructures as compared with the top-down approach. However, the alignment of nanostructure is a serious problem for applications of nanostructures.

This dissertation follows the style of *Fluctuation and Noise Letters*.

Conventional semiconductor processes are applied to nanostructure fabrication in the top-down approach. Usually, the fabrication of a quantum well is the starting point of the nanostructure fabrication. By use of molecular beam epitaxy or metal organic chemical vapor deposition technique, an ultra-thin single crystalline layer can be deposited on a bulk substrate. The development of these advanced epitaxy techniques makes it possible to fabricate single crystalline layer with a very fine boundary. Then, by e-beam lithography or photolithography process we can remove a part of the single crystalline layer and fabricate nanostructure. However, the top-down approach requires very expensive equipment.

Silicon-based integrated circuit (IC) industry has been developed according to Moore's law saying that every third (or second) year the size of a transistor shrinks four times smaller and the number of transistors per unit area increases by four times. The number of transistors per a chip has been doubled every second year from the 1970s to 2002. Intel introduced a new central processing unit (CPU) fabricated in a 90 nm process in 2004 [7], and Samsung Electronics started mass-production of a 1 Gbit dynamic random access memory (DRAM) chip using a 90 nm processes in 2005 [8]. That is, DRAM and CPU already include nanostuctures. Kish reported that the Johnson-Nyquist noise increases with shrinking the size of a metal-oxide-semiconductor field effect transistor (MOSFET) and that the noise limits the operation frequency of a chip as well as the number of transistors per chip at a given power [9, 10]. It suggests that electronic noise can restrict the hardware and operation conditions of nanoscale digital processors. Here, we expand his work in MOSFET processors to other nanoscale digital processors-single electron logic (SEL) and current-controlled digital processors. While two digital levels in MOSFET processors depend on many electrons, SEL processors depend on a single electron. Therefore, a single electron has to be controlled by the gate voltage of a transistor in SEL processors. Although MOSFET and SEL processors are voltage-controlled digital processors, current-controlled processors can be available in nanoscale digital processors. The effect of the Johnson Nyquist noise on current-controlled digital processors is similar to the effect on MOSFET processors. Thus, the shot noise effect will be discussed in current-controlled digital processors.

In general, a sensor consists of three parts, i.e., detection, signal amplification and signal analysis. When we call a sensor a nanosensor, the characteristic size of the detection part of the nanosensor is nanoscale. As mentioned before, since the nanoscale detection part is affected by a single or several analytes (biomolecule), the sensitivity of the nanosensor is enhanced. Moreover, whenever a single biomolecule affects the nanoscale detection part of the nanosensor, the detection part generates different types of stochastic signals from that of a background signal. Since a single biomolecule moves randomly in an analyte solution, the signals from the detection part include random fluctuations. Therefore, the signals from the nanosensor are stochastic signals. The properties of the stochastic signals reflect the random motion of analytes as well as the interactions between a single analyte and the detection part. Kish said about the properties that it is gold in the trash [11]. Fluctuation-enhanced sensing is one of signal analysis methods. The simplest version of the fluctuation-enhanced sensing is to analyze stochastic signal on the basis of power density spectra.

We demonstrated that the fluctuation-enhancing sensing method was useful to detect a bacterium with a sensing of phage-triggered ion cascade (SEPTIC) nanosensor [12]. Patolsky *et al*. reported that single viruses are detected by silicon nanowire (SiNW) nanosensors [13]. The signals generated by the SINW nanosensors are stochastic signals as expected. Here, we develop models for SEPTIC nanosensors and for SiNW nanosensors.

In chapter II, we take into consideration thermally-assisted tunneling effect in SEL processors and shot noise in current-controlled digital processors [14]. The influence of the electronic noise on the nanoscale digital processors is discussed. In chapter III, we introduce SEPTIC and SiNW nanosensors, discuss the physical sources of the fluctuation in the SEPTIC sensors, and develop a classical model for pH SiNW nanosensors. We summarize the electronic noise in nanostructures with respect to the limitation of nanoscale digital processors and the sensor applications and discuss further works in chapter III.

CHAPTER II

LIMITATION OF NANOSCALE DIGITAL PROCESSORS

Since 1999, IC microprocessors such as DRAM and CPU already include nanostructures as mentioned before. As the size of MOSFETs in the IC processors has shrunk, the number of transistors per unit area has increased exponentially and the operation frequency of the processors have increased at the same time. In 2002, Intel Pentimum IV included about one millions transistors and its operation frequency was 2 GHz [9].

Threshold level is required in digital processors since digital processors work in on and off levels since crossing the threshold level means switching between two levels. The two-level problem in digital processors is similar to the stochastic resonance problem. Moreover, problems on threshold-level-crossing in Gaussian noise are at the core of many stochastic phenomena. The Johnson-Nyquist noise, i.e., thermal noise and shot noise are Gaussian noise. Gingl, Kish and Moss reported that error rate and energy dissipation play a determining role in stochastic resonators [15]. It suggests that error rate and energy dissipation in nanoscale digital processors can also be important factors on threshold-level-crossing since nanoscale digital processors have electronic noise which is one of Gaussian noise. Since nanoscale digital processors usually will contain millions of transistors or more, energy dissipation in nanoscale processors becomes significant.

Kish took account of the Johnson-Nyquist noise effects on MOSFET processors [9]. The Johnson-Nyquist noise causes bit-flip errors in MOSFET processors. Taking these bit-flip errors into consideration, Kish found the safe thermal noise margin that threshold voltage has to be 12 times bigger than root-mean-square (RMS) thermal noise voltage. He also reported that the number of transistors per unit area and the operation frequency cannot increase at the same time at a given finite power dissipation in the MOSFET processors.

Single electron transistor (SET) is one of the next generation nanoscale transistors. It has two single electron junctions and one quantum dot as shown in Fig. 2.1. Two pre-requirements for the satisfactory on/off switching operation of a single ultrasmall junction are related to the capacitance, C, and the tunneling resistance, R_T, of the junction [16,17]. In the first place, the tunneling resistance of the ultrasmall junction has to be greater than the resistance quantum $R_K = h/q^2 \cong 25.8\ \mathrm{k}\Omega$, where h is the Plank constant and q is the elementary charge, since the energy uncertainty associated with the tunneling lifetime, $\tau_T = R_T C$, should be much smaller than the electrostatic charging energy $E_C = q^2/2C$. The other requirement is that the electrostatic charging energy has to be greater than thermal energy. The first condition leads to the observable discrete energy levels for single electron tunneling, and the second one to the blockade of the thermally assisted tunneling. The single electron tunneling has been observed at low temperatures (< 77 K) [18], where both requirements are easily satisfied by today's technology.

In single electron logic (SEL) processors, logic levels depend on whether a single electron exists (or passes). Averin and Likharev [17], and Korotkov [19] proposed SEL gates and circuitry. They used the SET as the basic component of these circuits. However, at non-zero temperature, thermally assisted tunneling takes place even at such voltages where the device would have closed at zero temperature, which apparently leads to bit-flip errors [17].

MOSFET-based and SEL processors are voltage-controlled digital processors. Although voltage-controlled digital processors are popular now, we can also use current-controlled digital processors for nanoscale processors. The influence of the Johnson-Nyquist noise on current-controlled digital processors is similar to voltage-controlled digital processors. However, since shot noise takes place with the electric current flowing in electronic devices, it can be important in current-controlled digital processors.

Here we consider two kinds of nanoscale digital logic processors—SEL and current-controlled digital processors. Neither of the processors is fabricated and available now. However, if single electron transistors are used as the basic components of nanoscale processors, both processors may be applied. In section 2.1, we introduce SEL processors and obtain the error-free performance condition at room temperature in the SEL processors. In section 2.2, we evaluate the error rate of a current-controlled digital processor where shot noise is dominant and discuss the limitation of the current-controlled digital processors. The same results in this chapter are reported in Ref. [14]

2.1. *SINGLE ELECTRON LOGIC PROCESSORS*

As mentioned before, two logic levels in SEL processors can be distinguished on the basis of whether a single electron passes through a single electron transistor (SET) shown in Fig. 2.1. The SET is a basic component in the SEL processors. However, SETs can also be substituted for MOSFETs as basic components in voltage- or current-controlled processors. Figure 2.1 shows

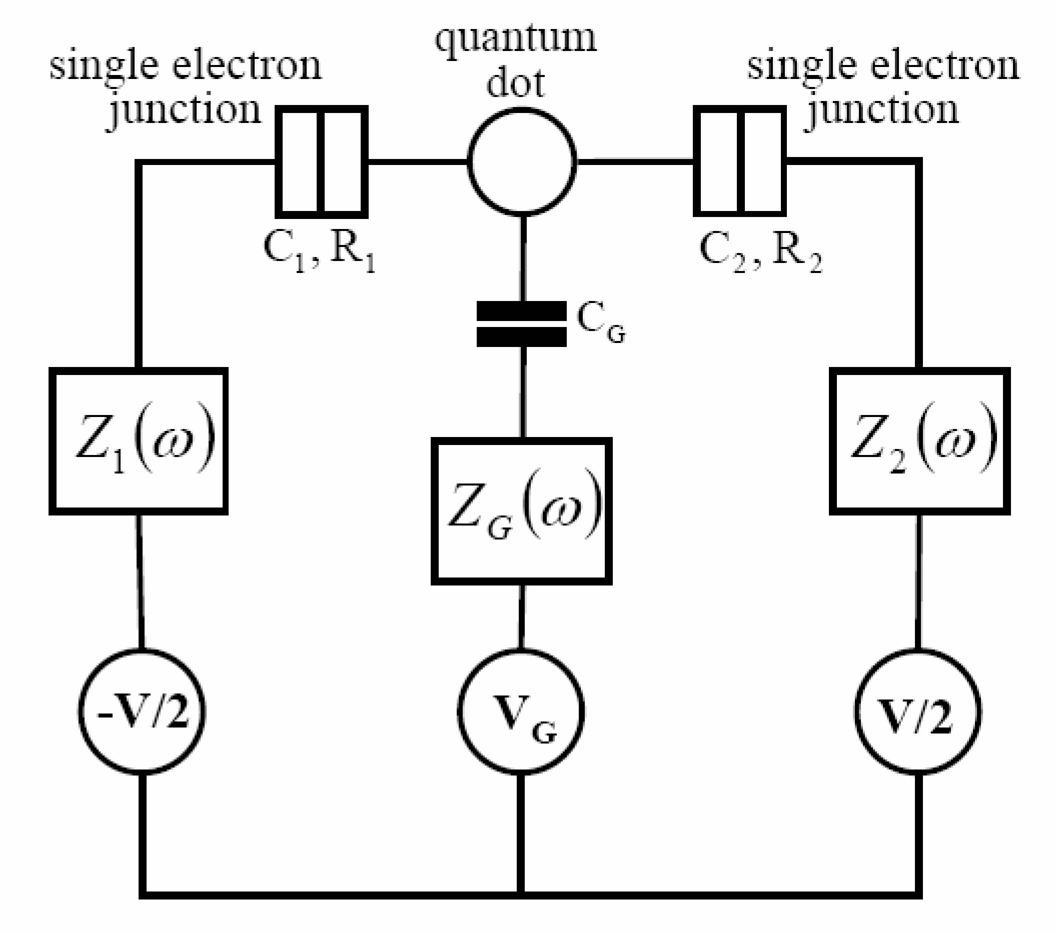

Figure 2.1. Schematic diagram of a symmetric single electron transistor. It consists of two single electron junction, one quantum dot and a single gate.

symmetric SET. It has two symmetric single electron junctions and one quantum dot. A single electron tunnels through single electron junction. The tunneling is controlled with gate voltage.

2.1.1. *Error-free performance condition*

Firstly, we consider a SET with double single electron junction, including a gate capacitor and a QD, with low impedance driving and outputting, i.e., $Z_1, Z_2, Z_G \langle\langle R_K, \omega^{-1}C_1^{-1}, \omega^{-1}C_2^{-1}, \omega^{-1}C_G^{-1}$, as shown in Fig. 2.1. Under these low-impedance conditions, the single electron tunneling rate through each junction is expressed as follows [20]:

$$\vec{\Gamma}_1 = \frac{1}{q^2 R_1}\frac{E_{1r}(V, V_G, n\,q)}{1-\exp[-\beta\, E_{1r}(V, V_G, n\,q)]} = \frac{k_B\,T}{q^2 R_1}\frac{\eta_{1r}}{1-\exp(-\eta_{1r})} \tag{2.1a}$$

$$\overleftarrow{\Gamma}_1 = \frac{1}{q^2 R_1}\frac{E_{1l}(V, V_G, n\,q)}{\exp[\beta E_{1l}(V, V_G, n\,q)]\ -1} = \frac{k_B T}{q^2 R_1}\frac{\eta_{1l}}{\exp(\eta_{1l})-1} \tag{2.1b}$$

$$\vec{\Gamma}_2 = \frac{1}{q^2 R_2}\frac{E_{2r}(V, V_G, n\,q)}{1-\exp[-\beta E_{2r}(V, V_G, nq)]} = \frac{k_B T}{q^2 R_2}\frac{\eta_{2r}}{1-\exp(-\eta_{2r})} \tag{2.1c}$$

$$\overleftarrow{\Gamma}_2 = \frac{1}{q^2 R_2}\frac{E_{2l}(V, V_G, n\,q)}{\exp[\beta E_{2l}(V, V_G, n\,q)]\ -1} = \frac{k_B T}{q^2 R_2}\frac{\eta_{2l}}{\exp(\eta_{2l})-1} \tag{2.1d}$$

where $\vec{\Gamma}$ and $\overleftarrow{\Gamma}$ are the single electron tunneling rates through the junction in a left-to-right and a right-to-left directions, respectively. The subscript number represents the different junctions, and the subscripts *r* and *l* represent the direction that an electron tunnels from left to right and from right to left, respectively. R is the tunneling resistance, $\beta = 1/k_B T$, and *n* is the number of the excess charges on the QD. The tunneling-related energies in Eq. (2.1) are defined by

$$E_{1r}(V, V_G, ne) = \frac{q}{C_\Sigma}\left[\left(C_2 + \frac{C_G}{2}\right)V + C_G V_G + nq - \frac{q}{2}\right] \tag{2.2a}$$

$$E_{1l}(V, V_G, ne) = \frac{q}{C_\Sigma}\left[\left(C_2 + \frac{C_G}{2}\right)V + C_G V_G + nq + \frac{q}{2}\right] \tag{2.2b}$$

$$E_{2r}(V, V_G, ne) = \frac{q}{C_\Sigma}\left[\left(C_1 + \frac{C_G}{2}\right)V - C_G V_G - nq - \frac{q}{2}\right] \tag{2.2c}$$

$$E_{2l}(V, V_G, ne) = \frac{q}{C_\Sigma}\left[\left(C_1 + \frac{C_G}{2}\right)V - C_G V_G - nq + \frac{q}{2}\right]\ , \tag{2.2d}$$

and the dimensionless energies η 's are defined by

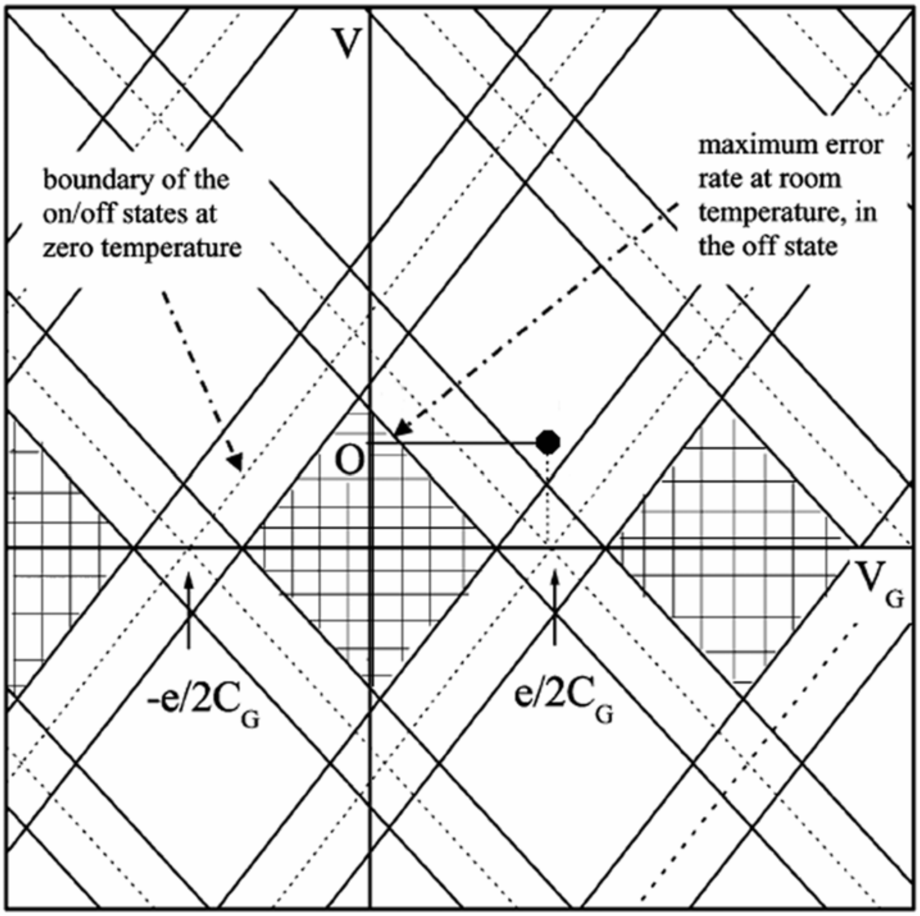

Figure 2.2. Stability diagram of a single electron transistor with asymmetric junctions. The point O represents 'off' state, and the black dot does 'on' states.

$$\eta_i(V, V_G, n\,q) = \beta E_i(V, V_G, n\,q) = \frac{E_i(V, V_G, n\,q)}{k_B T} \quad (i = 1r, 1l, 2r \text{ and } 2l) \quad . \tag{2.3}$$

Here, C_Σ is the sum of the capacitances, $C_\Sigma = C_1 + C_2 + C_G$. Equation (2.1) shows that the tunneling rate depends only on the dimensionless energy, η_i , and the tunneling resistance at fixed temperature. At a given tunneling resistance and temperature, Eq. (2.3) allows us to draw the different regimes of working, as shown in Fig. 2.2 as a function of the source-drain voltage, V and the gate voltage, V_G . The maximal error rate, one-bit-flip-error/year/system, is used as the condition of the error-free performance on Fig. 2.2. The dotted lines represent the boundaries between the 'on' and 'off' states at zero temperature, while the solid lines represent the conditions of the maximal error rate in the "off" state. Each region represents different tunneling combination. The checked regions represent the zero current regions, depending on the maximal error rate, and their area is temperature dependent (see Eq. (2.3)). These regions exist if the following conditions are satisfied simultaneously:

$$\eta_{jr}(V,V_G,nq) \le -\alpha_j^r(R_j,T) \quad \text{and} \quad \eta_{jl}(V,V_G,nq) \ge \alpha_j^l(R_j,T) \ , \tag{2.4}$$

where we call the α 's stability parameters. Equations (2.2), (2.3) and Relations (2.4) are used to generate Fig. 2.2.

Using Eqs. (2.1) and Eq. (2.4), the values of the α 's can be obtained from the following equations:

$$\frac{\Gamma^Y q^2 R_j}{k_B\, T} = \frac{-\alpha_j^r(R_j, T)}{1 - \exp\left[\alpha_j^r(R_j, T)\right]} \quad , \tag{2.5a}$$

and

$$\frac{\Gamma^Y q^2 R_j}{k_B\, T} = \frac{\alpha_j^l(R_j, T)}{\exp\left[\alpha_j^l(R_j, T)\right] - 1} \quad (j = 1 \text{ and } 2) \ , \tag{2.5b}$$

where Γ^Y is the maximal error rate. Since Eqs. (2.5a) and (2.5b) are the same functional form and generally $\exp[\alpha(R, T)] >> 1$, the α 's are approximated as

$$\alpha(R_j,T) \cong -\,\mathrm{W}\left(-\frac{\vec{\Gamma}^Y q^2 R_j}{k_B T}\right) \tag{2.6}$$

where $\mathrm{W}(x)$ is the Lambert W-function [21]. After substituting the parameter α , Eq. (2.6), into Eq. (2.4), the error-free performance condition is obtained from Eqs. (2.2) through (2.4) and (2.6):

$$\frac{q^2}{2C_\Sigma} > \alpha(R_T, T)\, k_B\, T \ . \tag{2.7}$$

Eq. (2.7) expresses the condition that a SET or a chip has the tunneling rate below the maximal error rate in the "off" state.

2.1.2. *Application of error-free performance condition*

At practical operation the two voltages, V and V_G, have to satisfy two different kinds of requirements. First, the drain voltage cannot be greater than $V^{\max}$ which corresponds to the maximal error rate in the "off" state. Second, in the "on" state, the gate should be driven by V_G^{opt} which provides the maximal possible current at given $V^{\max}$. In Ref. [22], simple considerations based on Eqs.(2.2) lead to:

$$V^{\max} = \min\left\{ \frac{2}{2C_1 + C_G}\left(\frac{q}{2} - \frac{\alpha_1^r C_\Sigma k_B T}{q}\right),\ \frac{2}{2C_2 + C_G}\left(\frac{q}{2} - \frac{\alpha_1^r C_\Sigma k_B T}{q}\right)\right\} \tag{2.8a}$$

and

$$V_G^{opt} = \frac{q}{2C_G} + \frac{\left[(2C_1 + C_G)\alpha_1 - (2C_2 + C_G)\alpha_2\right]\, k_B T}{2\, q\, C_G} \tag{2.8b}$$

where $\alpha_j = \alpha(R_j, T)$ and $\min(a, b)$ represents the minimum of a and b. If the two junctions are symmetric, i.e., $C_1 = C_2$, $R_1 = R_2 = R$, then Eqs. (2.8) will be simplified so that the operation voltages in the "on" state become $V^{\max} = q/2C_\Sigma$ and $V_G^{opt} = q/2C_G$. In this case, we have the maximal rate of electron flow through the device:

$$\vec{\Gamma}_t = \frac{1}{8\, C_\Sigma R\, \left[1 - \exp\left(-\beta\, q^2/4\, C_\Sigma\right)\right]} \cong \frac{1}{8\, C_\Sigma R} \quad . \tag{2.9}$$

Eq. (2.9) is based on unidirectional tunneling because tunneling in the reverse direction would be negligible at the maximal tunneling rate conditions. When the transistor runs at the maximal clock frequency, the dissipation power of a single SET with symmetric junctions is

$$P_1 = q \cdot \vec{\Gamma}_t \cdot V_G^{opt} = \frac{q^2}{16 C_G C_\Sigma R} \quad . \tag{2.10}$$

It is important to note that this is the ultimate lower limit of dissipation because Eq. (2.10) takes into account only the energy needed to control the device. The actual power dissipation of the device is not included in this picture because it can be dependent on several other conditions.

In general, a semiconductor SET is built in lateral structure which has 2-dimensional electron gas. In the lateral structure, the QD of the SET is supposed to be a flat circular disk. Therefore, using the size dependence of the geometric capacitance, $C_\Sigma = 8\varepsilon R_{QD}$ [23], we obtain the following relations for the size dependence of the error-free performance condition:

$$R_{QD} \le \frac{q^2}{16\varepsilon\alpha(R,T)\,k_B T} \quad , \quad \vec{\Gamma} \cong \frac{1}{64\varepsilon R_{QD} R} \quad , \quad P_1 = \frac{q^2}{128\varepsilon C_G R_{QD} R} \tag{2.11}$$

where ε is the permittivity of insulator and R_{QD} is the radius of a flat circular disk. Eq. (2.11) holds for any semiconductor SET with symmetric junctions.

Here, we regard the transistor packing density as $\theta = 0.01$, where θ is the ratio of the actual number transistors to the number of devices of the characteristic size at fully dense packing. From Eq. (2.11), the power dissipation of a chip with N SETs can be given as

$$P_N = N * P_1 = N\frac{q^2}{128\varepsilon C_G R_{QD} R} \approx \theta \frac{10^{-4}}{R_{QD}^2}\frac{q^2}{128\varepsilon C_G R_{QD} R} = \frac{10^{-4} q^2 \theta}{128\varepsilon C_G R_{QD}^3 R} \quad . \tag{2.12}$$

It should be noted that this is the lower limit of power dissipation of the chip because the dissipation of other elements are neglected.

Figure 2.3 shows the lower limit of power dissipation of a single SET and *N* SETs (when running at the maximal clock frequency) and the maximal clock frequency of the single SET. Here, $\varepsilon = 3.9\varepsilon_0$ for SiO$_2$, $R = 1\text{M}\Omega$ and $C_G / C_\Sigma = 0.1$ are assumed. It is apparent from Eqs. (2.11) and (2.12) and from the slope of curves in Fig. 2.3 that $f_{MAX} \propto R_{QD}^{-1}$, $P_1 \propto R_{QD}^{-2}$, and $P_N \propto R_{QD}^{-4}$. It is important to point out that the power dissipation limits of chips, which is about 100 W, sets another upper limit for the clock frequency. When the maximal power dissipation of a chip is limited at 100 W, the radius of the QD and the maximal clock frequency are about 6 nm and 30 GHz, respectively. It implies that the processors built with SETs of $R_{QD} \le 6\text{nm}$ cannot operate at the maximal clock frequency f_{MAX} .

Finally, we study the maximal quantum dot size as a function of an operation temperature. The results are compared by a simple prediction based on the level-crossing analysis of thermal noise at given capacitance and bandwidth [20]. The rms thermal noise voltage $V_n = \sqrt{k_B T / C_G}$ on the capacitor and the practical noise margin $V_G^{opt} \ge 12 V_n$ used in [9] yields the following relation:

$$C_G \le \frac{1}{576}\frac{q^2}{k_B T} \quad . \tag{2.13}$$

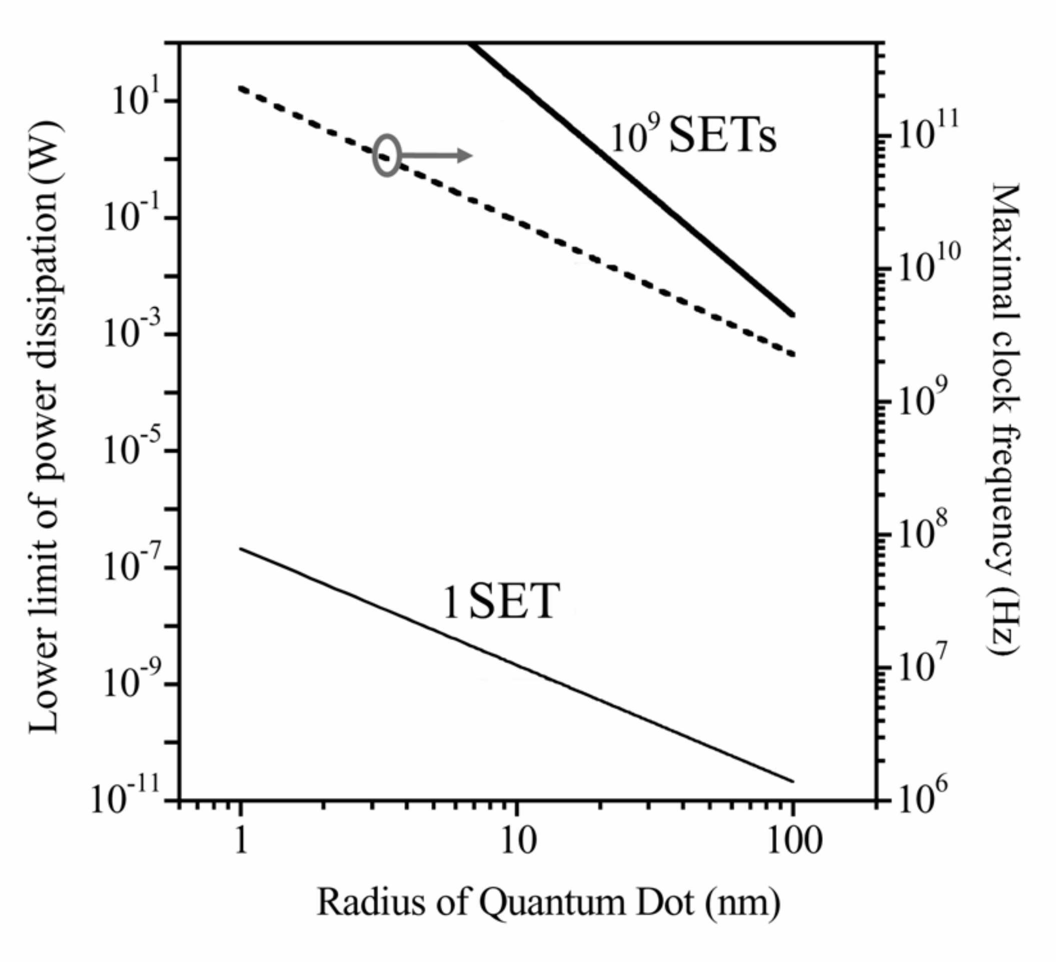

Figure 2.3. Lower limit of power dissipation and the maximal clock frequency. These are evaluated in a single electron logic processor with a single electron transistor or *N* single electron transistors. The transistor packing density is assumed to be 0.01 as current microprocessors.

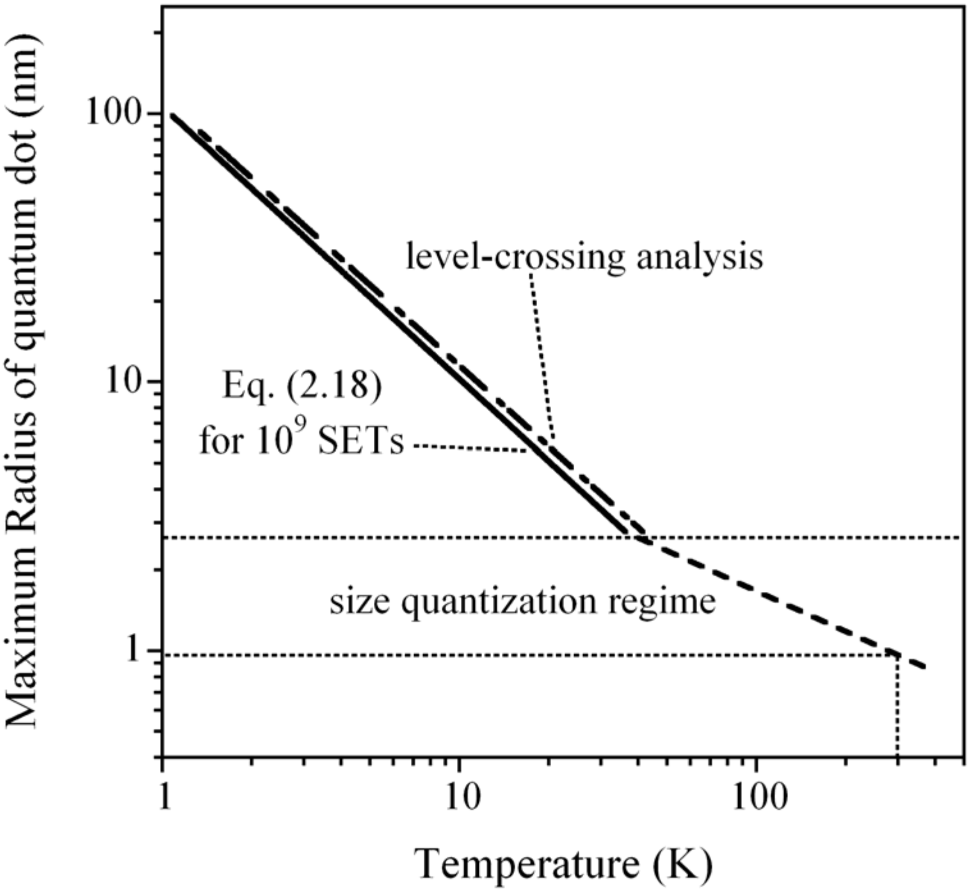

Figure 2.4. Maximum radius of quantum dot in the single electron transistor. It is evaluated when the single electron logic processor works within the maximal error rate at a given temperature.

Surprisingly, it is shown in Fig. 2.4 that the simple thermal noise estimation works very well at large QD limit. However, as the size of the QD decreases, the size quantization effect becomes dominant. The ratio of energy level spacing in quantum dot to electrostatic charging energy is given by

$$E_{QD} \big/ E_C = 4\pi\hbar^2 C_\Sigma \big/ m_e q^2 A_{QD} \tag{2.14}$$

where m_e is the effective mass of the electron and A_{QD} is the area of the quantum dot. The radius of the QD is 2.77 nm for Si/SiO$_2$ in the case which the ratio is unity. The energy level spacing from the size-quantization effect is proportional to $1/R_L^2$ where R_L is the characteristic length of the QD. Since thermal energy is much less than the spacing among energy levels, the maximum characteristic length of the QD satisfies $\log(R_L)_{MAX} \propto (-1/2)\log T$. Therefore, the case that the size-quantization effect is dominant has a different slope due to $T \propto R_{QD}^{-1/2}$. That is, the size quantization effect is a beneficial effect which helps to work at higher temperatures or larger sizes. The analysis of Fig. 2.4 suggests that a SEL processor including 10^9 SETs with smaller than 1 nm QD size can work at room temperature.

The aspects of power dissipation and error-free performance have been studied as a function of the radius of QD. The analysis shows that nanoprocessors with silicon QDs of less than 1nm radius can be used at room temperature in SEL processors. The most important conclusion is that a single electron nanoprocessor working at room temperature has to be in the size quantization working mode.

2.1.3. *Summary*

In this section, we considered the single electron logic (SEL) processors consisting of single electron transistors (SET). It was shown that the thermally-assisted single electron tunneling can lead to bit-flip errors. We obtained the error-free performance condition. Applying the error-free performance condition, we showed that power dissipation in the SEL processors limits the maximal clock frequency at a given power and that the silicon based SEL processors have to include SETs of about 1nm radius quantum dot for room temperature operation.

2.2. *CURRENT-CONTROLLED DIGITAL PROCESSORS*

In the previous section, we discussed SEL processors. The MOSFET digital and SEL processors are voltage-controlled. Here, we discuss current-controlled digital processors. Inductors in current-controlled processors play the role of gate capacitor in the MOSFET processors, and the property of the Johnson Nyquist noise in an inductor is the same as in a capacitor from the functional point of view. Therefore, it is reasonably expected that the error-free performance condition in current-controlled processors is the same as in the MOSFET processors if the Johnson Nyquist noise is dominant. The current-controlled processors has another noise source, i.e., shot noise; when the electric current flows in electronic devices, the shot noise is observed with the Johnson-Nyquist noise. Current shows random fluctuations since it consists of discrete electronic charges. The shot noise is different from the Johnson-Nyquist noise since the Johnson-Nyquist noise can take place without applied voltage but the shot noise cannot. In this section, we consider current-controlled digital processor where the shot noise is dominant.

2.2.1. *Maximal clock frequency and information channel capacity*

We consider a current-controlled digital processor. As mentioned before, we assume that the shot noise is dominant in the processor. As in MOSFET processors with voltage-controlled logic [9], we assume that the noise margin is 60 % of the 'on' state current as in the best possible case. It means that the threshold current is 60 % of the 'on' state current.

The mean frequency for the amplitude of a Gaussian noise to cross the zero level is given by the Rice formula. Kish generalized the Rice formula to evaluate the mean frequency for the amplitude of a Gaussian noise to cross an arbitrary level [24]. The generalized Rice formula is given by

$$\nu(u_{th}) = \frac{2}{\sigma} \exp\left(-\frac{u_{th}^2}{2\sigma^2}\right)\sqrt{\int_0^\infty f^2 S(f)df} \tag{2.15}$$

where ν is the mean crossing frequency, σ is the standard deviation of the Gaussian noise, u_{th} is the threshold level, and $S(f)$ is the power spectrum density of the noise.

If the shot noise is a full shot noise, the one-sided power density spectrum (PDS) of the shot noise is $2Iq$, where I is the current and q the elementary charge. Since the PDS is independent of frequency, the shot noise is white noise. The operation clock of the digital processor is the cutoff frequency f_c. For a single gate of the current-controlled processor, generalized Rice formula yields the error rate

$$\nu_f(I, f_c) = \frac{2}{\sqrt{3}} f_c \exp\left(-\frac{9}{100}\frac{I}{f_c q}\right) \tag{2.16}$$

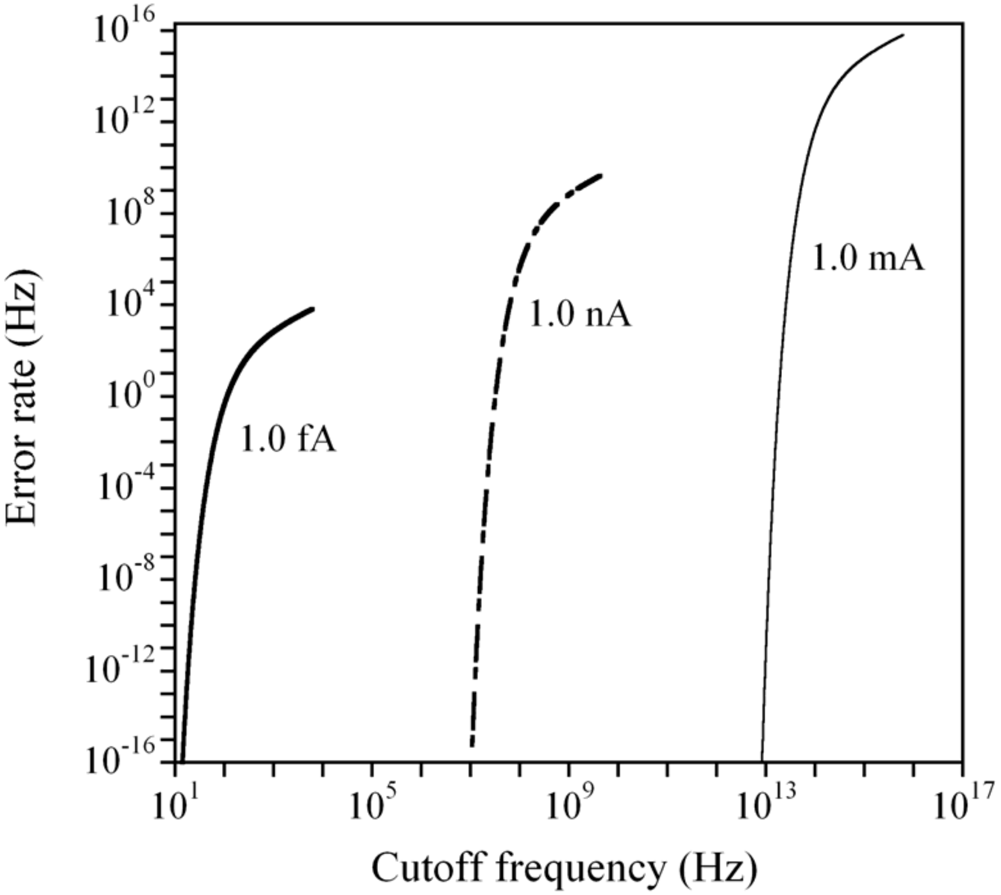

Figure 2.5. Dependence of the error rate of a single gate on the cutoff frequency. Each number in a figure represents the operation current.

The cutoff frequency is roughly equal to the highest possible clock frequency of the processor. It is shown in Fig. 2.5 that the error rate increases very rapidly with the cutoff frequency.

For a processor including N elements, the error-free performance condition is that the error rate for the single gate is no less than f_{year}/N where f_{year} is the maximal error rate of a chip. Therefore, using Eq. (2.16), the maximum error rate is given by

$$\frac{f_{year}}{N} = \frac{2}{\sqrt{3}} f_{c,\max} \exp\left(-\frac{9}{100} \frac{I}{q\, f_{c,\max}} \right) \tag{2.17}$$

where $f_{c,\max}$ is the available maximum cutoff frequency. The acceptable maximum error rate per year of a chip for upper limit of noise-induced error rate is one bit error/chip/year, i.e.,

$f_{year} = 3.17 \times 10^{-8}\,\mathrm{Hz}$. By using Eq. (2.17) and the definition of the Lambert W-function [21], the available maximum cutoff frequency, $f_{c,\max}$, is obtained by

$$f_{c,\max} = \frac{\sqrt{3}}{2} \frac{f_{year}}{N} \exp\left[\mathrm{W}\left(\frac{3\sqrt{3}}{50} \frac{I}{q} \frac{N}{f_{year}} \right) \right] \tag{2.18}$$

where $\mathrm{W}(x)$ is the Lambert W-function. Since $\mathrm{W}(x) \cong \ln x - \ln(\ln x)$ at $x >> 3$, the maximum cutoff frequency is approximated as

$$f_{c,\max} = \frac{9}{100} \frac{I}{q} \left[\ln\left(\frac{3\sqrt{3}}{50} \frac{I}{q} \frac{N}{f_{year}} \right) \right]^{-1} . \tag{2.19}$$

The maximum cutoff frequency is a good estimation of the maximal clock frequency of the processor with the maximal error rate. Figure 2.6 shows the maximal clock frequency as a function of the operation current. The thin solid line represents the maximal clock frequency of the single element and the thick solid line represents that of the digital processor including 100 million elements. It is apparent that the maximal frequency is almost independent of the number of the elements in the processor. As shown in Fig. 2.6, Eq. (2.19) can be used in the both cases. It is shown that the highest maximal clock frequency would be 10 GHz in the processor with 10^8 transistors if a maximal supply current is 100 A.

Information channel capacity of a single channel is given by Shannon information formula [25]

$$C_1 = B \ln\left(1 + P_{signal}/P_{noise}\right) \tag{2.20}$$

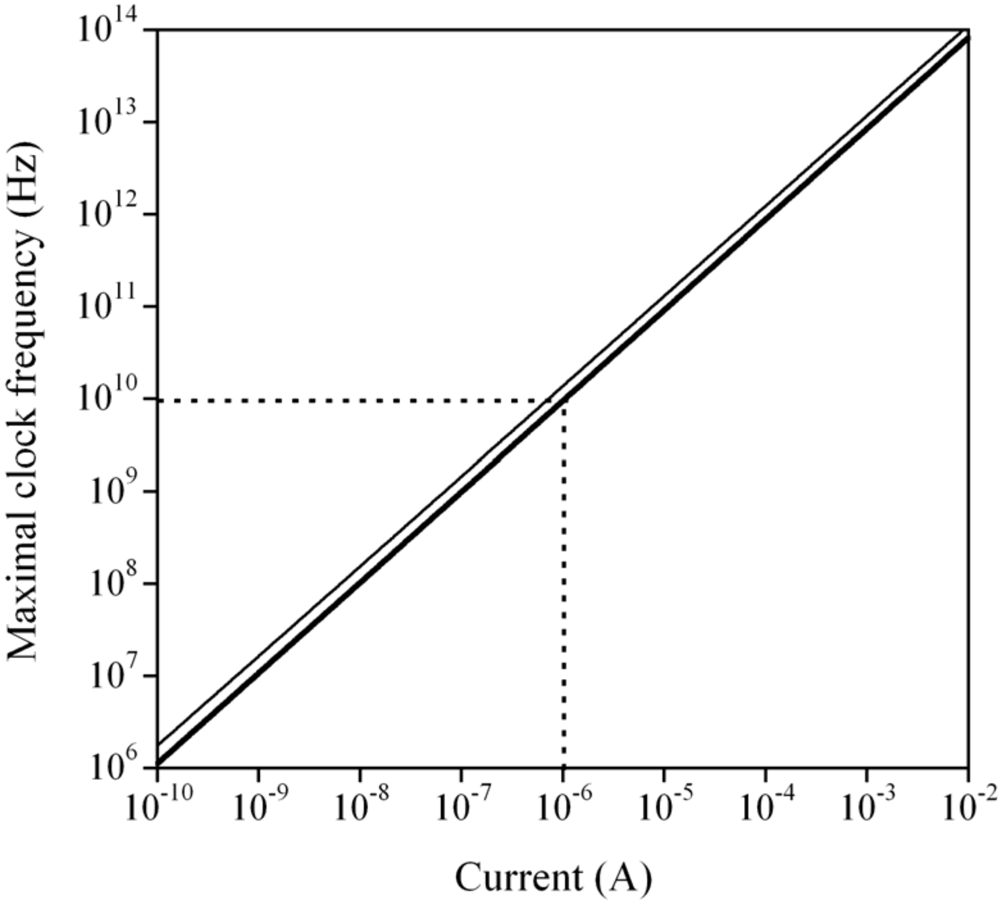

Figure 2.6. Maximal clock frequency as a function of the operation current. The solid lines and the dashed lines are obtained from Eqs. (2.18) and (2.19), respectively. The thick lines represent the processor including 10^8 transistors but the thin lines a single transistor.

where B is the bandwidth of signal which can be approximated by the clock frequency in the processor, and P_{signal} and P_{noise} are the powers of the signal and of noise, respectively. Since the signal is a square wave, P_{signal}/P_{noise} is approximated as the ratio of the clock frequency to the error rate. Supposed that all transistors operate independently, the upper limit of information channel capacity is rewritten as

$$C = N\, f_{c,\max} \ln\left(1 + \frac{f_{c,\max} N}{f_{year}}\right) \tag{2.21}$$

Figure 2.7 shows the information channel capacity at the maximal clock frequency. As shown in Figs. 2.6 and 2.7, both of the maximum clock frequency and the information capacity increase monotonically with increasing the operation current.

2.2.2. *Summary*

We took into consideration the current-controlled digital processor where the shot noise is dominant. It is shown that the bit-flip error rate caused by the shot noise increases very rapidly with the cutoff frequency and that the power dissipation limits the maximal clock frequency.

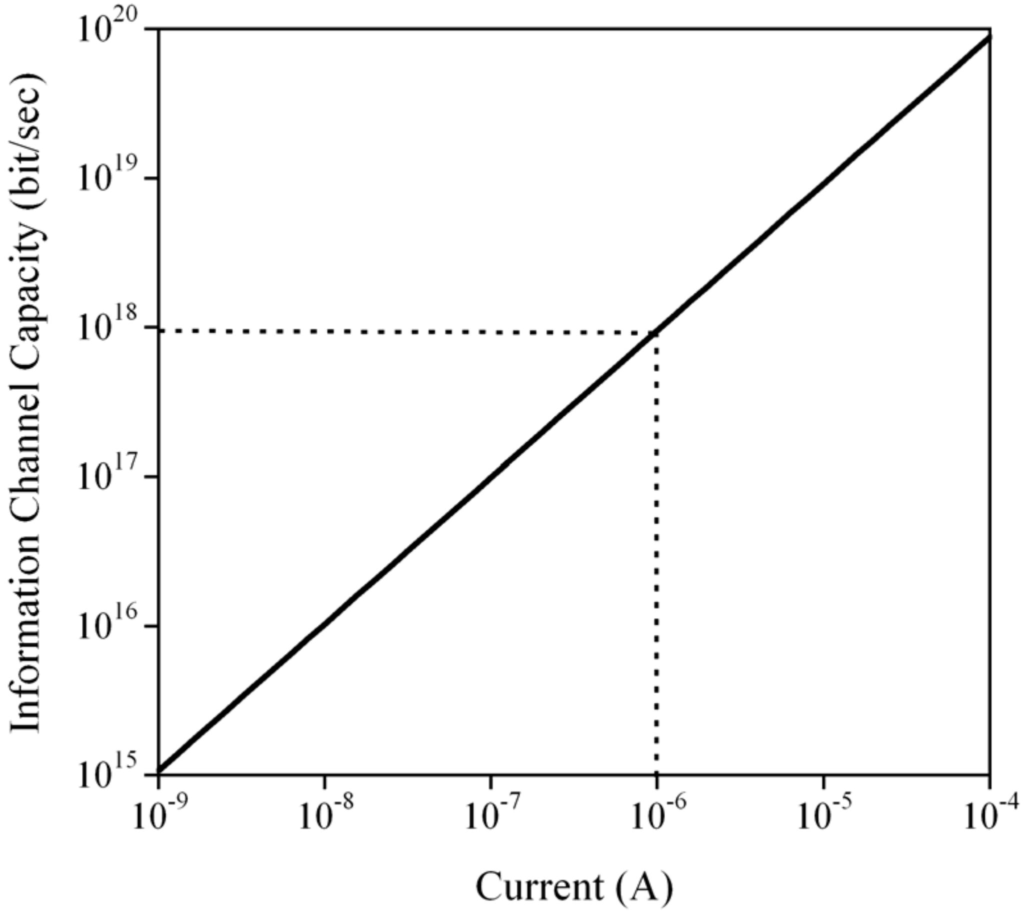

Figure 2.7. Information channel capacity at the maximal clock frequency. It is evaluated in the current-controlled logic processor with 10^8 transistors. The possible operation condition of the processor is a current range of less than 10^{-6} A if the maximal supply current is 100 A.

CHAPTER III
SENSING APPLICATIONS

Great interest in the biomedical applications of nanotechnology has been grown in the last decade. Especially electrical nanosensors to detect biological macromolecules such as virus, bacteria, RNA, and DNA, are one of the promising biomedical applications of nanotechnology since they are faster, more selective and more sensitive than any conventional biological analysis technologies.

Several biological analysis technologies are available for the identification of bacteria in human, veterinary and agricultural diagnosis. Classical metabolic profiling, diagnostic polymerase chain reaction (PCR), and fatty acid content are all widely used and commercialized methods [26-28]. However, these technologies require well-equipped laboratory environments. As well, the time spent in obtaining definitive analytical results is of the order of magnitude of hours to days since the bacteria must be grown in pure culture and then subjected to analysis. PCR is somewhat less subject to the problems, but it cannot distinguish between living and dead bacteria. Therefore, it is important to research rapid and inexpensive methods for detecting and identifying living bacteria suitable for large-scale field environments.

Recently, two electrical nanosensors have been reported; one is a sensing of phage-triggered ion cascade (SEPTIC) nanosensor [12] and the other is silicon nanowire (SiNW) nanosensor [13]. It is expected that both nanosensors are implemented inexpensively and that both nanosensors spend shorter time in analysis than conventional technologies.

As mentioned before, the detection part of nanosensors is so sensitive that it detects analytes (i.e., biomolecules) on molecular levels. However, the detection part generates stochastic signals which have random fluctuations. Since the random fluctuations are hidden in a background signal, the information detected by the nanosensors could be ignored without caution. The fluctuation-enhanced sensing (FES) method can increase the sensitivity and the selectivity of the nanosensors since it extracts fluctuation information on analytes from the stochastic signals. The simplest version of the FES method is the power density spectrum of analytes-induced voltage fluctuations [29]. It was demonstrated that the FES method can enhance the sensitivity and the selectivity of commercial gas sensors for various chemicals [30,31]. Another version of the FES method is the use of higher-order statistics such as bispectrum introduced in Appendix.

In the SEPTIC nanosensor, bacteriophage-infected bacteria release potassium ions and move randomly at the same time; therefore, the SEPTIC nanosensor generates random fluctuations, i.e., stochastic signals.

The SiNW nanosensors are able to detect all kinds of biomolecules [4,5]. Since a specific receptor corresponding to a specific biomolecule can be immobilized at the surface of the SiNW, the selectivity of the nanowire sensor is controlled by the choice of the specific receptor. It was reported that single viruses are detected without sample purification and that fluctuations occur when a single virus is bound at the surface of the SiNW [12]. The operation of the SiNW nanosensors is qualitatively understood. However, it is difficult to quantitatively analyze nanosensors due to complex solid-solution interface at the surface of the SiNW and the electronic properties in the SiNW.

In section 3.1, we demonstrate that an FES with nano-gap metal probes, so called a SEPTIC nanosensor, is applicable to detect a single bacterium via bacteriophage infection. As well, we analyze the physical source of the fluctuations in the SEPTIC nanosensor. In section 3.2, SiNW nanosensors are introduced and we develop a classical quantitative model for a pH SiNW nanosensor.

3.1. *SENSING OF PHAGE-TRIGGERED ION CASCADE SENSORS*

Bacteriophages (sometimes, called phages) are the most numerous biological entities; that is, the number of phages is estimated to be 10^{31} on the earth [32]. Phages exist with a wide range of host specificities from narrow host range phages, infecting only some strains of *E. coli*, to generalists, injecting the phage's DNA into enterobacteria and myxobacteria [33, 34]. Attempts to make use of phages in detection and identification of pathogenic bacteria have required culturing the target bacteria, growing the infected culture, and assaying the production of progeny virions in a traditional way. It takes at least several hours to complete these processes.

The bacteriophage infection is irreversible adsorption. For double-stranded DNA phages, the bacteriophage infection begins with interactions between the specific adsorption apparatus (usually tail fibers) and specific receptors on the surface of a host cell [35]. The interactions lead to the transitory formation of a channel through which the phage's DNA passes into the host cell [36]. After that, potassium ions release from the infected host cell at a rate of about 10^6 ions/s [37]. If we detect the bacteriophage infection phenomenon at a single bacterium level, we can identify bacteria due to the host specificities in bacteriophage. Moreover, the identification method takes relatively very short time compared to a traditional technique since the bacteriophage infection can occur in seconds and no analyte (target cells) culture is necessary.

3.1.1. *Experiments and results*

The nano-gap titanium probes are shown in Fig. 3.1. The titanium thin film was deposited 20 nm thick on a $LiNbO_3$ substrate. The part of the titanium film was etched into two pieces, and most of the area of the two titanium films was covered with AZ5214 photoresist. We removed a part of the photoresist and made the 8 μm × 6 μm window as shown in Fig. 3.1. Thus, two titanium probes of about 4 μm × 4 μm were exposed to air. The gap between two titanium probes is 150 nm wide. The analyte solution wets two titanium probes through the window. We connect the probes to a preamplifier (Stanford Research System, SR560) and measure the difference between two probes.

All bacteria for experiment were derivatives of *E. coli* K-12 W3110 [38]. The λ^S and λ^R strains were W3110 Δ*fhuA* and W3110 Δ*fhuA* Δ*lamB*, respectively (both $T5^R$), and the $T5^S$ strain was W3110 *gyrA*(Nal^R) Δ*fhuB*. The following phages are used: λΔ(*stf tfa)::cat cI857 S105* (λPaPa) lacking side tail fibers, Ur-λ having 4 side tail fibers from R. Hendrix and T5 from I. Molineux.

Analyte bacteria were grown in Luria broth at 37 °C, washed and resuspended in 5 mM $MgSO_4$. The basic experimental procedures were as follows: (1) to mix 10 μL of a CsCl-purified phage stock at a titer of about 10^{10} pfu/mL with the equal volume of the suspension of sample bacterial cells, (2) to incubate at 37 °C for various times as indicated, (3) to apply 5 μL of the mixture to the nano-gap probes, and (4) to measure voltage difference between two probes over a 2 min period.

After a sample droplet of about 5 μL was applied to the nano-gap probes, the voltage signal generated from the probes was amplified with the preamplifier, and then the power density spectrum $S_u(f)$ was measured over a 2 minute interval with a dynamic signal analyzer (Stanford Research System, SR785). Our initial experiments used two siphophages of *E. coli* with well-known outer membrane receptors-the temperate phage λ requiring LamB and the virulent phage T5 requiring FhuA [39,40]. When mixtures of either phage with sensitive bacteria were tested with the nano-gap probe device, large and slow stochastic fluctuations were observed in time domain. The fluctuations had an approximately $1/f^2$ power spectrum in a frequency range of 1-

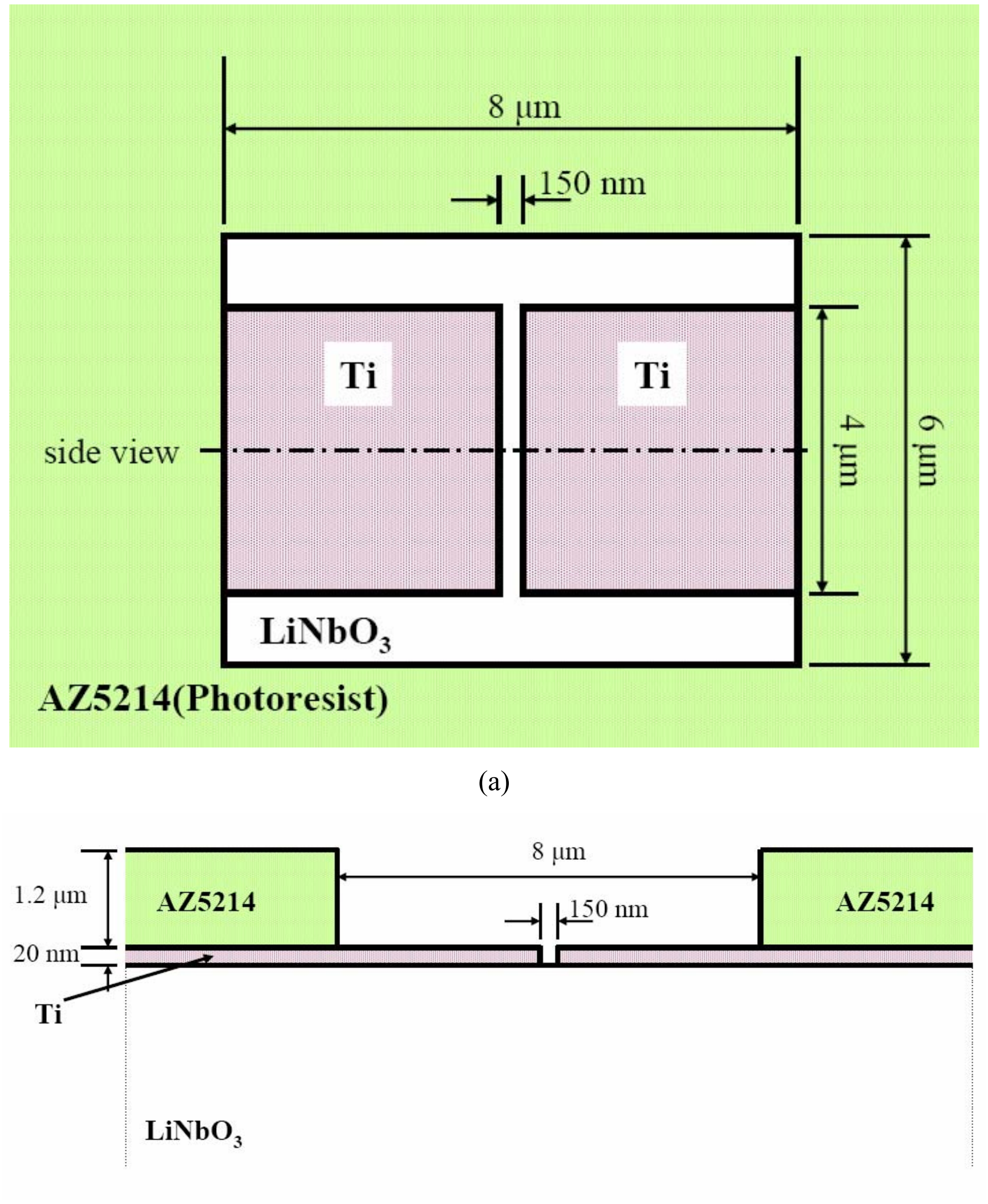

(a)

(b)

Figure 3.1. Schematic diagram of the nano-gap metal probes; (a) top view and (b) side view. The sample droplet is placed on the metal probes.

10 Hz as shown in Fig. 3.2. In contrast, the spectrum of voltage fluctuations in mixtures of the same phage with isogenic Δ*lamB* (λ^R) bacteria follows an $1/f$ noise. This is consistent with background voltage noise spectra caused by two possible origins - the corrosion of the titanium probes and the input current noise of the amplifier. If slow redox corrosion takes place in an electrode system, the power spectra can be $1/f$ noise [41,42]. The input current noise of the amplifier is proportional to the square of the impedance of the nano-gap, and thus small variations in the conductivity of the solution can cause observable changes in the noise level [43]. Much higher amplitude fluctuations were observed for the adsorption of phage T5 to sensitive cells and they showed an $1/f^2$ power spectra; However, control mixtures with isogenic Δ*fhuA* ($T5^R$) cells show only the $1/f$ background as shown in Fig. 3.2. The λ phage used for these experiments was derived from the standard laboratory parental strain λPaPa, constructed decades ago [44]. However, λPaPa lacks side tail fibers and adsorbs much more slowly to sensitive cells than the original wild-type λ (Ur-λ) does [44]. When Ur-λ was used in these experiments, much higher amplitude fluctuations with a frequency dependence of approximately $1/f^2$ were observed, beginning about 1 minute after mixing and increasing for about 5 minutes as shown in Fig. 3.3. It may happen since all the phages spent time in being adsorbed. It is also shown in Fig. 3.3 that identical control experiments with resistant bacteria unable to adsorb Ur-λ yielded the $1/f$ background noise.

To understand the influence of the probe size on the stochastic signal, two large titanium probes of 100 μm gap was also tested. The micro-gap probes were fabricated by deposition and lithography of titanium thin film. Since the titanium probes are not covered with the photoresist, the contact area of the analyte solution on the micro-gap probes is about 500000 times greater than that on the nano-gap probes. As shown in Fig. 3.4, the amplitudes of the power density spectra were much smaller and the power density spectra of mixtures of phages with sensitive and resistant bacteria were identical. Many infected bacteria can be close to the large contact-area micro-gap probes at one time while a few infected bacteria can be near the nano-gap probes. It indicates that many infected bacteria may average out the voltage fluctuations at the micro-gap probes at the large contact-area micro-gap probes. Thus, it is a reasonable thought that the voltage fluctuations happen when the infected bacteria are close to the probes.

During the processes of DNA injection by a siphophage or a myophage, each irreversibly-adsorbed virion opens a single channel in the cytoplasmic membrane, through which the DNA

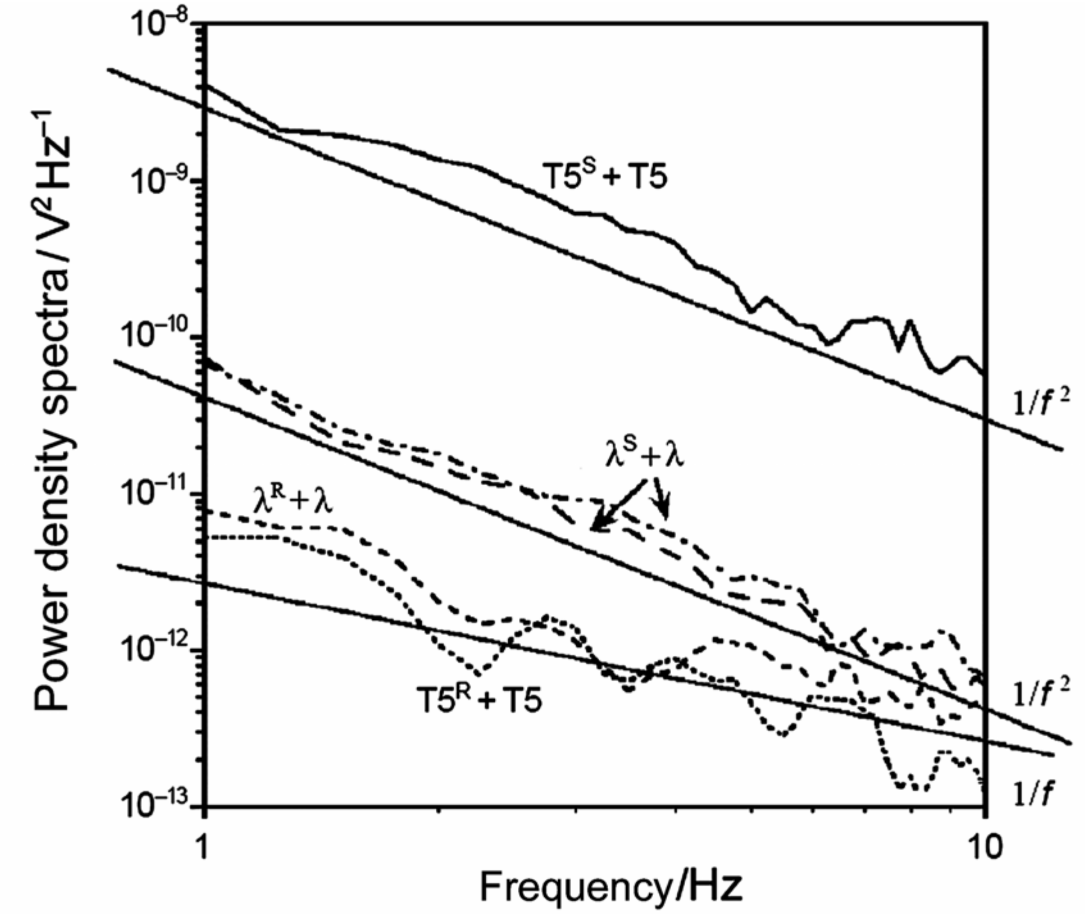

Figure 3.2. Power density spectra measured during 2 minutes for mixtures of bacteria and phages at the nano-gap probes. Straight lines indicate *1/f* or *1/f* ^{2} slope. Phage λ infects λ^S or λ^R cells, and phage T5 does $T5^S$ or $T5^R$ cells.

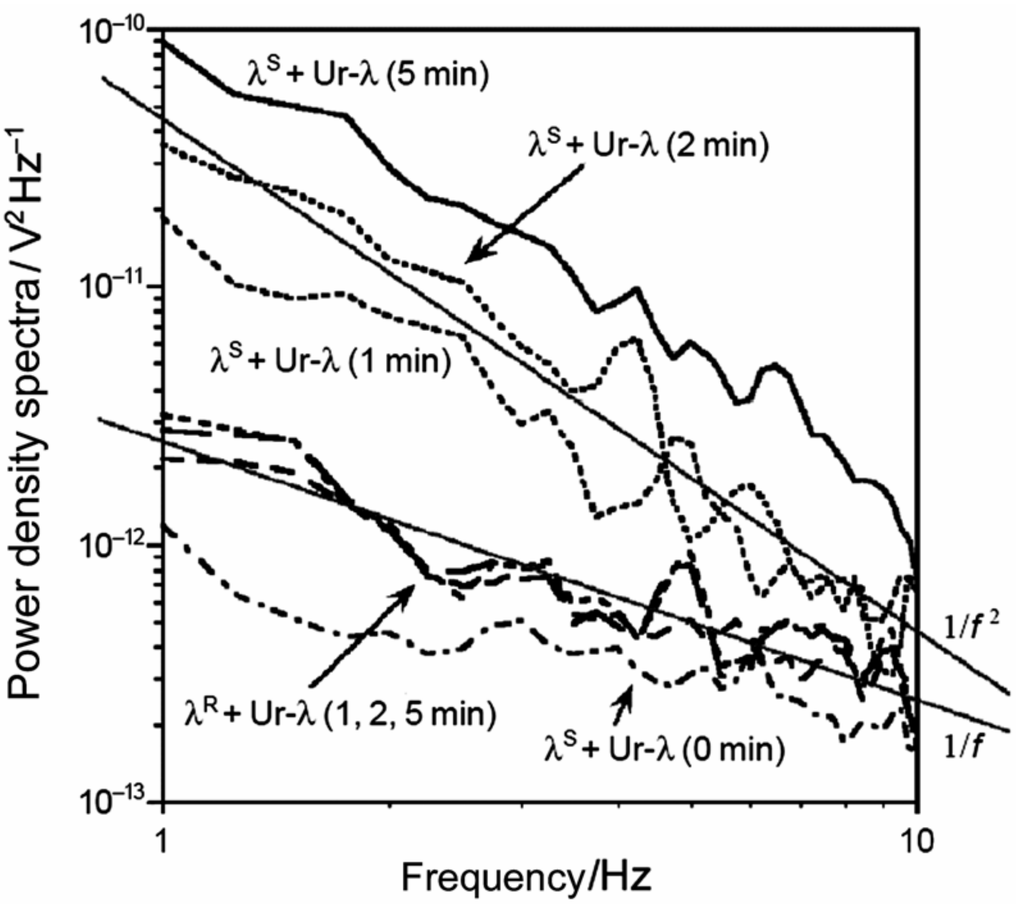

Figure 3.3. Pre-incubation time influence on power density spectra. The power density spectra measured during 2 minutes for mixtures of bacteria and the original wild-type λ phage, Ur-λ, at the nano-gap probes. The indicated times are pre-incubated time.

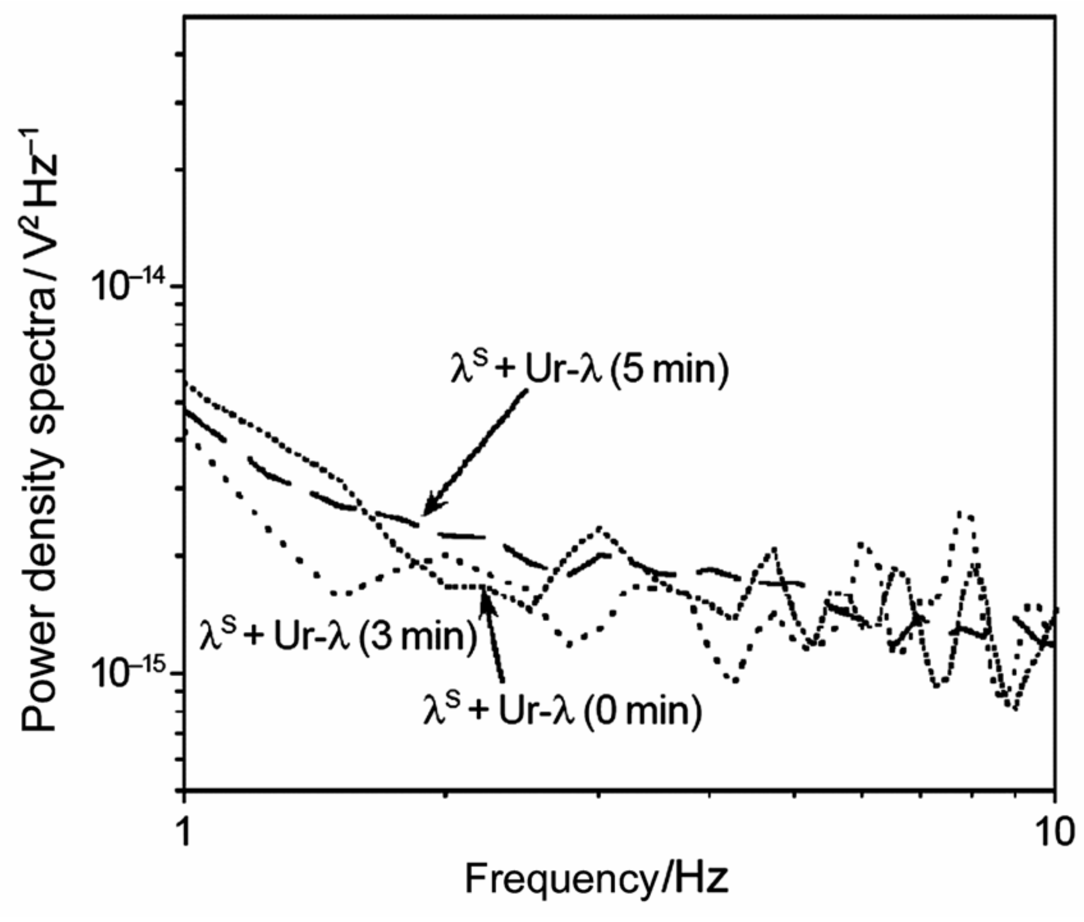

Figure 3.4. Power density spectra measured with two micro-gap probes. They were measured during 2 minutes for mixtures of bacteria and the original wild-type λ phage, Ur-λ. The indicated times are pre-incubated time.

molecule of the phage passes. It was reported that the DNA injection leads to transient cellular depolarization and Potassium ion release of about 10^6 ions per infected cell per second [37]. The released ions undergo Brownian motion around the infected cell. The randomness of the ion diffusion may generate spatiotemporal electrical field fluctuations at micrometer or sub-micrometer scale.

The above results show that the SEPTIC nanosensor can apply for the highly specific detection of bacteria on a scale of a few minutes without culturing the bacteria. The additional advantage of the SEPTIC nanosensor is that only living cells, which have energized membranes, will be detected. From the overall point of view, the fluctuation, i.e., stochastic signal is generated since the bacteriophage-infected bacteria release potassium ions and move randomly at the same time. Kish et. al discussed the detection limitation of the SEPTIC sensors [45]. They thought of the source of the $1/f$ background noise as the input impedance of the amplifier for voltage measurement in Ref. [45]. However, the more specific sources and the quantitative consideration of the $1/f^2$ stochastic signals are required to optimize the SEPTIC design.

3.1.2. *Effect of the released potassium ions on the fluctuation*

In this section, we discuss the diffusion of the released potassium ions from the infected cells as a function of time and position and whether it can generate the stochastic signal.

To evaluate the concentration profile of the released potassium ions around the infected cell, we assume that *E. coli* cells in the analyte solution have the same properties of spherical colloid particles in our electrolyte solution. Due to the spherical symmetry of the spherical colloid particle, the concentration profile is given by time-dependent drift-diffusion equation [46]

$$\frac{\partial n(r,t)}{\partial t} = \frac{1}{r^2}\frac{\partial}{\partial r}\left\{ r^2 \left(D_{K^+} \frac{\partial n(r,t)}{\partial r} - \mu_{K^+} F(r,t) n(r,t) \right) \right\} \tag{3.1}$$

where $n(r)$ is the concentration of the released potassium ions as a function of radius, D_{K^+} is the diffusivity of the potassium ions, μ_{K^+} is the mobility of the potassium ions, and $F(r,t)$ is the electric field around the cell. Even though there are many kinds of ions outside of the cell and the potassium ions released from the cell, magnesium ion and sulfate ion concentrations in the analyte solution are dominant and the other ion concentrations can be ignored. Therefore, the released potassium ions cannot affect the electric field around the cell. However, as we will mention later, the zeta potential of the infected cell is varying with the potassium ions released.

The Debye-Hückel approximation, which is available at the small zeta potential, gives the electric field around the cell by [47]

$$F(r,t)=\zeta(t)a\frac{1+\kappa r}{r^2}e^{-\kappa(r-a)} \tag{3.2}$$

where κ is the inverse Debye length defined by

$$\kappa=\left(\frac{q^2\sum n_k^0 z_k^2}{\varepsilon_0\,\varepsilon_r\,k_B\,T}\right)^{1/2} \tag{3.3}$$

where n_k^0 and z_k are the bulk number concentration and the valency of the ion of type k. At 25°C in an aqueous solution, the value of κ is simply given by

$$\kappa=\left(\frac{2000\,\mathscr{F}^2}{\varepsilon_0\,\varepsilon_r\,RT}\right)^{1/2}\sqrt{S_{ion}}=3.288\times10^9\sqrt{S_{ion}}\;(\mathrm{m}^{-1}) \tag{3.4}$$

where $\mathscr{F}$ is Faraday's constant (= 96485.3383 C/mol) and S_{ion} is the ionic strength defined by $S_{ion}=\sum_k c_k\,z_k^2/2$. Here c_k is the concentration of the ion of type k (in unit of 10^3 mol/m^3). As mentioned above, magnesium ion and sulfate ion concentrations are dominant in the solution. Thus, by using Eq. (3.4), the value of the inverse Debye length in 5 mM $MgSO_4$ solution is obtained to be $\kappa=0.464\times10^9\ \mathrm{m}^{-1}$. The Debye length is about $2.16\times10^{-9}\ \mathrm{m}$. The electric field varies strongly inside the Debye length, but it is almost zero outside of the Debye length. Since the Debye length is about 2 nm, we ignore the drift-term in Eq. (3.1) and rewrite Eq. (3.1) as

$$\frac{\partial n(r,t)}{\partial t}=\frac{1}{r^2}\frac{\partial}{\partial r}\left\{r^2\left(D_{K^+}\frac{\partial n(r,t)}{\partial r}\right)\right\} \tag{3.5}$$

To solve Eq. (3.5), we need the boundary conditions. Since the potassium ions release from the infected cell, the boundary condition at the surface of the cell is

$$-4\pi a^2 D_{K^+}\frac{\partial n}{\partial r}=J_{K^+}\quad \text{at } r=a \text{ and } 0<t<t_{efflux} \tag{3.6}$$

where J_{K^+} is the release rate of the potassium ions, $J_{K^+}=10^6$ ions/sec, and t_{efflux} is the time when the potassium ions release from the infected cell. The concentration profile around a cell is affected by the released potassium ions from other cells after the potassium ions diffuse across half of the mean distance between two infected cells; thus, the boundary condition on the other side is dependent on time. Before the time, the boundary condition is given by

$$n(r,t)=0\quad \text{at } r\to\infty \text{ and } 0<t<t_{cross}\quad , \tag{3.7a}$$

and after the time, the boundary condition is written as

$$\frac{\partial n(r)}{\partial r} = 0 \quad \text{at } r = R_{middle} \text{ and } t > t_{cross} \quad . \qquad (3.7b)$$

where R_{middle} is half of the mean distance between two infected cells in the analyte solution, and t_{cross} is the time when the potassium ions diffuse across half of the mean distance between two infected cells. R_{middle} is obtained approximately as 6.2×10^{-6} m by using the concentration of the *E. coli* cells in the analyte solution. The initial condition for Eq. (3.5) is $n(r, t = 0) = 0$. Let's introduce dimensionless parameters: $u = n/n_0$, $\tau = D_{K^+}\, t/a^2$, $x = r/a$, and $j_0 = J_{K^+}/4\,\pi\, a\, n_0\, D_{K^+}$ where n_0 is the maximum concentration of the released potassium ions in the analyte solution. Rewriting Eq. (3.5) with the dimensionless parameters, applying Laplace transform to Eqs. (3.5) and (3.6), and solving the ordinary differential equation yield

$$\hat{u}(x, s) = \frac{j_0}{x} \frac{e^{-\sqrt{s}(x-1)}}{s\left(\sqrt{s} + 1\right)} \quad . \qquad (3.8)$$

Applying inverse Laplace transform to Eq. (3.8) and rewriting the concentration with dimension parameter, we obtain the concentration of the released potassium ions as a function of position and time as follows:

$$n(r, t) = \frac{J_{K^+}}{4\,\pi\, a\, D_{K^+}} f_{transient}(r, t) \qquad (3.9a)$$

where $f_{transient}(r, t)$ is given by

$$f_{transient}(r, t) = \left\{ Erfc\left(\frac{r - a}{2\sqrt{D_{K^+}\, t}} \right) - Erfc\left(\sqrt{\frac{D_{K^+}\, t}{a^2}} + \frac{r - a}{2\sqrt{D_{K^+}\, t}} \right) \cdot \exp\left(\frac{r - a + \sqrt{D_{K^+}\, t}}{a} \right) \right\} \quad . \qquad (3.9b)$$

Here, $Erfc(x)$ is the complementary error function. $f_{transient}(r, t)$ shows the transient behavior of the released potassium ions. The diffusivity of the potassium ions is $2 \times 10^{-9}\ \mathrm{m^2/s}$ [47] and the radius of the *E. coli* cell is approximately 0.5×10^{-6} m. Figure 3.5 shows the transient behavior of the potassium ions. The solid and dashed lines represent, respectively, $r = 2.0\ \mu\mathrm{m}$ and $r = R_{middle} = 6.2\ \mu\mathrm{m}$. It is shown that the potassium ions arrive at half of the mean distance between two cells, $r = R_{middle} = 6.2\ \mu\mathrm{m}$, at one millisecond and the concentration increases monotonically and becomes the steady state. Thus, $t_{cross} = 0.001\,\mathrm{second}$. It suggests that the potassium ions diffuse into the whole solution very fast and the other boundary condition (3.7b) has to be applied during most of the measuring time (2 minutes).

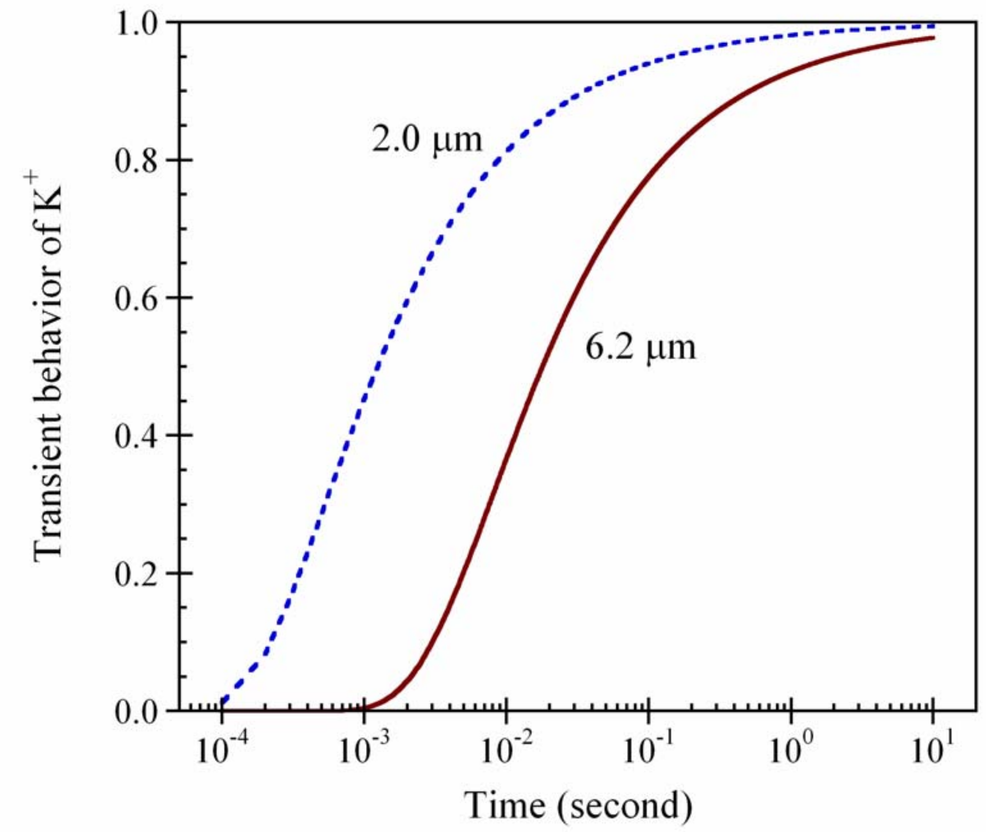

Figure 3.5. Transient behavior of the potassium ions based on Eq. (3.9b). The solid and dashed lines represent, respectively, $r = 2.0\ \mu\text{m}$ and $r = R_{middle} = 6.2\ \mu\text{m}$.

To manifest the effect of the released potassium ions on the voltage fluctuations, we need to solve the time dependent drift-diffusion equation with the boundary conditions, Eqs. (3.6) and (3.7b). We solve the equation numerically with the '*pdepe*' function in MATLAB to include the drift term in Eq. (3.1). The initial condition is $n(r, t = 0) = 0$ for the numerical calculation. It is acceptable since the amount of the released potassium ions is negligible during an interval of (0, 0.001 ms). The concentrations of the released potassium ions at $t = 60\,\text{seconds}$ and $t = 120\,\text{seconds}$ are uniform in the solution. It is noted that the electric field in the diffusion layer does not delay the diffusion of the released potassium ions seriously. The boundary condition Eq. (3.7b) is satisfied under the assumption that all infected cells release potassium ions at the same time. It is not true, but the result of this calculation suggests that the diffusion of the released potassium ions cannot generate the voltage fluctuations while the infected *E. coli* cells moves randomly far from the probes.

3.1.3. *Electrophoretic effect in the SEPTIC sensor*

As mentioned before, we observed large and slow isolated fluctuations in time domain during the measurement. The isolated fluctuation peaks can take place when an *E. coli* cell moves nearby the titanium probes. An isolated fluctuation peak can give $1/f^2$ power density spectrum [41]. However, since the amplitude of the power density spectrum is very small, we need many isolated fluctuation peaks during the measurement interval to observe the fluctuation effect in the power density spectrum. In this section, we qualitatively discuss the motion of the *E. coli* cells and the rate of the isolated fluctuation peak occurrence.

Biard and Kish took into consideration the motion of an *E. coli* cell in the SEPTIC sensor to investigate the way to enhance the sensitivity of the sensor [48]. However, their calculation is applicable only to extremely dilute electrolyte solution since they did not consider electrophoretic effect on the cell. Since the analyte solution includes 5 mM $MgSO_4$ electrolyte at the SEPTIC experiment, a model for the SEPTIC sensors has to include electrophoretic effect.

Electrophoresis is the motion of colloids in an electrolyte solution under the electric field [49, 50]. Here, we assume that *E. coli* cells in the analyte solution have the same properties of spherical colloid particles in an electrolyte solution since the *E. coli* K-12 cells are immotile. In electrophoresis, the velocity of the colloid particles v is proportional to the electric field strength E. Thus, the velocity of the cell is given by

$$v = \mu_E \, E \tag{3.10}$$

where μ_E is the electrophoretic mobility of the cell. Henry calculated μ_E for a spherical colloidal particle with arbitrary double layer thickness on the assumption that the charge density in the double layer is unaffected by the applied electric field [51,52]. This assumption is available if the ζ -potential (i.e., the potential at the outer Helmholtz plane) and the electric field are sufficiently low. He gives the formula for the electrophoretic mobility by

$$\mu_E = 2\frac{\varepsilon_0 \, \varepsilon_r}{3\eta}\zeta \, f_1(\kappa \, a) \tag{3.11}$$

where ε_0 and ε_r are, respectively, the vacuum permittivity and the relative dielectric constant of the electrolyte solution, η is the viscosity of solution, ζ is the zeta-potential, κ is the inverse Debye length in the electrolyte defined by Eq. (3.3), a is the radius of a colloidal particle and $f_1(\kappa \, a)$ is Henry's function for the retardation effect on the electrophoresis of spherical colloid particle. $f_1(\kappa \, a)$ is a monotonically varying function; it increases from 1.0 at $a = 0$ to 3/2 at $a \to \infty$ at a given electrolyte concentration (i.e., constant κ). The original form of $f_1(\kappa \, a)$ is not simple, but Ohshima proposed a simple approximate expression for $f_1(\kappa \, a)$ with relative errors less than 1% as [52,53]

$$f(\kappa \, a) = 1 + \frac{1}{2\left[1 + \dfrac{2.5}{\kappa \, a\left\{1 + 2\exp(-\kappa \, a)\right\}}\right]^3} \tag{3.12}$$

As calculated before, the value of the inverse Debye length in 5 mM $MgSO_4$ solution is $\kappa = 0.464 \times 10^9 \ \mathrm{m}^{-1}$. If the radius of an *E. coli* cell is $a = 0.5 \times 10^{-6}$ m, $\kappa \, a = 232$. By using Eq. (3.12) in Eq. (3.11) and the value of $\kappa \, a$, the electrophoretic mobility for the analyte solution is

$$\mu_E = 0.9895\frac{\varepsilon_0 \, \varepsilon_r}{\eta}\zeta \quad . \tag{3.13}$$

and then by using Eq. (3.13) in Eq. (3.10), the velocity of an *E. coli* cell in the electrolyte solution under the electric field is rewritten as

$$v = \left| 0.9895\frac{\varepsilon_0 \, \varepsilon_r}{\eta}\zeta \, E \right| \tag{3.14}$$

We need to know the zeta potential and the electric field to determine the velocity of the cell. First of all, let's estimate lower limit of the electric field strength with the dc current. Our experiment shows the parasite dc current between two probes is $I_{dc} = 1 \times 10^{-12} \ \mathrm{A}$. The real current in the electrolyte solution must be larger than the parasite current due to the existence of the electrolyte ions passing by the probes. Since the length of each square probe is about 4×10^{-6} m, the current density is 0.0625 A/m^2. The conductivity of $MgSO_4$ solution at 25 °C is evaluated by using empirical Casteel-Amis four-parametric equation [54]

$$\sigma_{MgSO4} = 5.802\times\frac{m}{1.823}\times\exp\left[-0.05307(m-1.823)^2-0.81787\frac{m-1.823}{1.823}\right] \tag{3.15}$$

where m is the molality, i.e., moles of electrolyte per kilogram of solvent. We can calculate the conductivity in molarity since we can calculate molality with molarity [55]. Using Eq. (3.15) for 5 mM $MgSO_4$, we obtain the conductivity is 0.03 (1/Ω/m). Applying Ohm's law, the effective electric field strength E is 2.1 V/m. Unfortunately the electrical structure and properties of an *E. coli* K12 cell is not well known such as dielectric constant inside the cell, surface charge densities at inner and outer cell membrane. Since the zeta potential is dependent on the potassium ion release, the zeta potential of the *E. coli* cell is regarded as a variable. Figure 3.6 shows the velocity of the *E. coli* cell as a function of the absolute value of the zeta potential. It is shown that the velocity rises about 0.1 to 0.3 μm/s when the absolute value of the zeta potential increases 50 to 200 mV. Since the bacterium current density is proportional to the velocity of the cell, it increases with the absolute value of the zeta potential. The increase of the bacterium current density results in the increase of the fluctuation peak occurrence rate and the amplitude of the power density spectrum.

3.1.4. *Summary*

We demonstrated a bacterium diagnostic technology by the use of the nano-gap probes combining the fluctuation-enhanced sensing and the specificity of bacteriophages. It is shown that the effect of the released potassium ions through the bacteriophage infection is negligible and that the bacterium current density and the power density spectrum in the phage infection case are larger than the non-infection case due to the electrophoretic effect in the SEPTIC sensors.

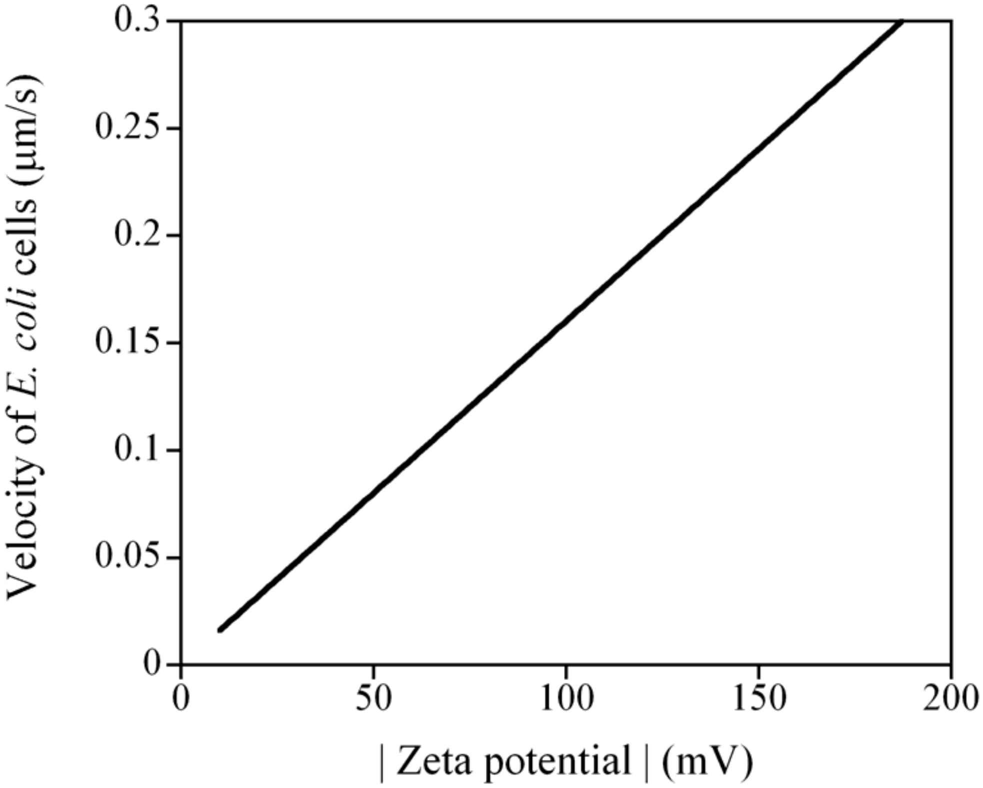

Figure 3.6. Lower limit of drift velocity of *E. coli* cells in our electrolyte solution under the effective electric field. The zeta potential can be thought of the surface potential of *E. coli* cells.

3.2. *SILICON NANOWIRE NANOSENSORS FOR VIRUS DETECTION*

Recently, the synthesis and the applications of SiNWs were reported [4,5]. The SiNWs applicable to chemical and biological nanosensors were synthesized by vapor-liquid-solid technology consisting of chemical vapor deposition with gold nanoclusters of 20 nm diameter, silane, and diborane as a p-type dopant [56-58]. The SiNW nanosensors are so ultra-sensitive that a single virus can be detected [13]. The schematic diagram of chemical and biological nanowire sensors is shown in Figure 3.7. The width of the microfluidic channel is about 2 or 3 μm. It was reported that the SiNWs have single-crystal silicon cores covered with 1–3 nm of amorphous oxide. The SiNW was heavily doped with p-type dopant and its conductance is from 200 to 1700 nS.

The SiNW nanosensors have been used to detect single viruses, protein and DNA sequences [13,56-58]. In order that the nanosensors can detect a single virus, the surface of the nanowire was modified by antibody receptor such as mAb receptors, anti-hemagglutinin for influenza A and anti-adenovirus group III. The antibody receptors are bound covalently at the surface of the silicon oxide. As a single virus passes by the surface-modified nanowire, it is combined reversibly with the receptors at the surface of the SiNWs. Since randomly a single virus adsorbs on and desorbs from the surface, the SiNW nanosensors give a stochastic signal in terms of the conductance. We can enhance the sensitivity and selectivity of the SiNW nanosensors by use of FES.

3.2.1. *Simple model for pH silicon nanowire nanosensors*

Since the SiNW nanosensor has electrolyte-insulator-semiconductor (EIS) structure, its sensing mechanism may be similar to that of EIS FET sensors [59]. At the EIS FET sensors, a sample solution comes in contact with the gate oxide surface of an n-channel (or p-channel) metal-oxide-semiconductor (MOS) FET. If surface charges at the gate oxide surface of the EIS FET sensors are regarded as the gate voltage of the MOS FETs, then the operation principle and the current-voltage characteristics of the EIS FET sensors are the same as the MOS FETs. Similarly, the current versus source-drain voltage characteristics of the SiNW nanosensors may be the same as the backside-gate SiNW FETs. However, we need to take into account the trans-conductance of the SiNW FETs since the origin of the gate effect in case of the SiNW nanosensors is different compared to the SiNW FETs.

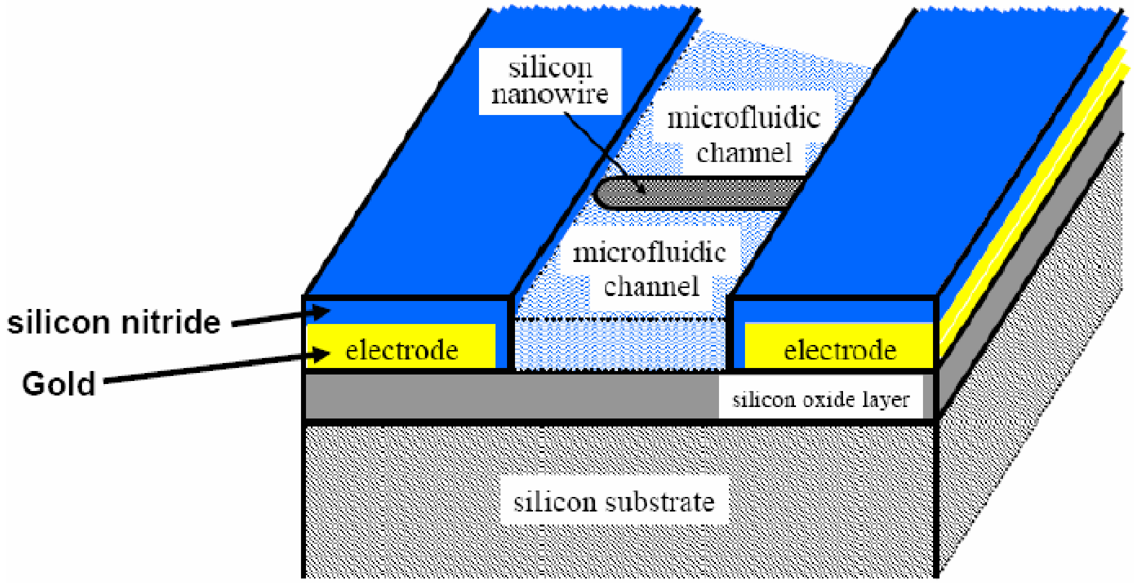

Figure 3.7. Schematic diagram of silicon nanowire sensors. The sample solution flows in microfluidic channel and virus in the sample solution adsorbs on the silicon nanowire.

Electrolyte-oxide interfaces consist of a special structure known as the electrical double layer (EDL) [49,50,60]. The EDL can be described by several models such as Gouy-Chapman model, Gouy-Chapman-Stern (GCS) model and the triple layer model (TLM). When Fung et al. developed the generalized theory of an EIS FET, they used the TLM to describe the electrolyte-oxide interface [60]. Here, we will also use the TLM.

The SiNW of the sensor consists of a single crystal silicon core (SC) covered with a 1–3 nm silicon oxide layer. It was reported that the contact between the SiNW and the metal electrode (source or drain) was Ohmic and that the current versus source-drain voltage characteristics of the backside-gate SiNW FETs were linear at room temperature [61,62]. It was also reported that the pH-dependence of the conductance in the SiNW nanosensor was in qualitative agreement with surface charge density at silicon oxide surface [13]. However, no quantitative model for the SiNW nanosensors has been developed.

We consider a pH SiNW nanosensor of which the SiNW is covered with unmodified surface oxide layer. The SiNW is submerged in a sample solution dissolving a monovalent electrolyte such as sodium chloride. Figure 3.7 shows the schematic diagram of the pH SiNW nanosensor. Voltage difference is biased at two metal electrodes (source and drain), and the source-drain voltage difference drives current through the SiNW. The sample solution flows in the microfluidic channel and wets the SiNW. Protonation or deprotonation at the oxide surface of the SiNW changes the current.

First of all, we discuss electronic transport inside the SC. Obviously, since the diameter of the SiNWs is about 10 nm, size quantization effect can exist. Therefore, since the lowest conduction and the highest valence bands of bulk silicon are shifted and split into subbands at the same time, the SiNWs are quasi-one-dimensional and its energy gap is larger than that of bulk silicon. However, the doping density of silicon quantum wires can reduce subband spacing and blue shift [63]. At low temperature, we can observe quantized or at least nonlinear conductance in the nanowire. However, it was reported that the current versus source-drain voltage characteristics of the backside gate SiNW FETs were observed to be linear at room temperature in spite of the 5 nm radius of the SiNW and that the contact between metal electrode and the SiNW of the backside gate SiNW FETs was Ohmic. These can be caused by thermal energy since thermal energy can spread holes into the subbands at equilibrium, which is named thermal smearing effect. Thus, the quantum effect disappears and one cannot observe the quantum effect at room temperature. Since holes occupy the subbands, it is reasonably assumed that the hole density is independent of the radial position without gate voltage. Since the diffusion-drift model can be used to explain these observations, we use it for the electronic transport in the SiNW as follows [46]:

$$j(r) = j_p(r) = q\,\mu_p\, p(r)F - qD_p \frac{\partial p}{\partial z} \tag{3.16}$$

where $j(r)$ is the total current density, j_p is the current density caused by holes, μ_p is the hole mobility, $p(r)$ is the hole density in the SC, D_p is the diffusivity of holes in the SC, and F is the electric field in the z-direction given by $F = V_{sd}/L$; here, V_{sd} is the voltage difference between source and drain; L is the length of the SiNW. Here, electron current density is ignored since the SC is p-type. Since the longitudinal length of the SiNW is 300 times longer than the radius, the longitudinal derivative of the electric field is negligible compared with the radial. Therefore, the electric field in the longitudinal direction can be regarded to be constant. Since the electric field and the current density in the longitudinal direction are constant, the longitudinal deviation of the hole density as well as the diffusion term of the current density can be ignored. Then, by integral of Eq. (3.16), current through the SiNW is presented by the following equation:

$$I = q\,\mu_p\, F\int_0^{R_c} p(r) 2\pi\, r\, dr \tag{3.17}$$

where R_c is the radius of the SC. Meanwhile, the electric displacement for p-type silicon is given by

$$\nabla \bullet \mathbf{D} = q\left[p(r) - N_a\right] \tag{3.18}$$

where $\mathbf{D}$ is the electric displacement; and N_a the concentration of acceptors. Applying the divergence theorem to Eq. (3.18) yields

$$R_c\, D_r(R_c) \equiv R_c\, \sigma_c = q\left[\int_0^{R_c} p(r) r\, dr - \frac{R_c^2}{2} N_a\right] \tag{3.19}$$

Substituting the integral of Eq. (3.19) in Eq. (3.17) leads to the current through the SiNW as

$$I = \pi\, q\,\mu_p \frac{V}{L} R_c^2\, N_a\left(1 + \frac{2\sigma_c}{q\, R_c\, N_a}\right) \quad , \tag{3.20}$$

and the conductance in the SiNW nanosensor is given by

$$G = I/V = G_0 + 2\pi\ \mu_p\, R_c\, \sigma_c / L \tag{3.21}$$

where $G_0 = \pi\, q\, \mu_p\, R_c^2\, N_a / L$ is the conductance of the SiNW without surface effects. The first term on the right hand side of Eq. (3.21) is independent of a sample solution but the last term is affected by it. we will call the parameter σ_c virtual-charge-density-at-the-silicon-oxide-interface (VCDSOI) since it is not charge density. If the VCDSOI is positive, the conductance increases; otherwise, the conductance decreases. That is, when the surface charge is negative and induces positive charges at the silicon-oxide interface, the VCDSOI is positive and the conductance increases. It is possible that quantum capacitance and surface charges affect transconductance in the SiNW nanosensors. John et al. reported that quantum capacitance can be neglected at low biased source-drain and source-gate voltages in long-channel, i.e., phase-incoherent carbon nanotube field effect transistors [64]. Generally quantum capacitance and the influence of the surface charges on mobility result in nonlinear transconductance. However, it was reported that the dependence of the transconductance of the SiNW on the surface charges is linear [61]. Therefore, those effects are negligible in the SiNW nanosensors.

We need to calculate the hole density and the electrostatic potential inside the SC. The hole density is expressed by

$$p(r) = n_i \exp\left[-\frac{q(\psi(r)-\varphi)}{k_B T}\right] \quad , \tag{3.22}$$

and the electrostatic potential inside the SC is given by

$$\frac{1}{r}\frac{d}{dr}\left(r\frac{d\psi}{dr}\right) = -\frac{q}{\varepsilon_0\,\varepsilon_{\mathrm{Si}}}\left(p(r) - N_a\right) \tag{3.23}$$

where n_i is the intrinsic-carrier density, ψ is the electrostatic potential, φ is the potential corresponding to the Fermi energy of intrinsic silicon, $\varepsilon_{\mathrm{Si}}$ is the dielectric constant of silicon. Hereafter, all of the electrostatic potential is in reference to bulk sample solution. Using Eq.(3.22) in Eq. (3.23) and introducing a perturbed electrostatic potential defined by $\psi = \psi_b + \tilde{\psi}$ yield

$$\frac{1}{r}\frac{d}{dr}\left(r\frac{d\tilde{\psi}}{dr}\right) = -\frac{q\,N_a}{\varepsilon_0\,\varepsilon_{\mathrm{Si}}}\left[\exp\left(-\frac{q\tilde{\psi}}{k_B T}\right) - 1\right] \tag{3.24}$$

Here ψ_b satisfies $n_i \exp\left(-q(\psi_b - \varphi)/k_B T\right) = N_a$ and corresponds to the Fermi energy of extrinsic silicon, and $\tilde{\psi}$ represents the potential variation caused by the surface charges. The potential inside the SC satisfies the following boundary conditions:

$$\tilde{\psi}(0) \sim \text{finite} \qquad \text{at the center} \tag{3.25a}$$

and

$$\tilde{\psi}(R_c) = \psi_c \qquad \text{at } r = R_c \tag{3.25b}$$

where ψ_c is the electrostatic potential at the silicon-oxide interface in reference to bulk sample solution. Assuming that the exponential term can be approximated such as $\exp(x) \approx 1 - x$, i.e., the Debye-Hückel approximation and solving Eq. (3.24) with Eq. (3.25), we obtain the potential inside the SC as

$$\tilde{\psi}(r) = \psi_c \mathbf{I}_0(\eta r)/\mathbf{I}_0(\eta R_c) \qquad \text{at } 0 \le r \le R_c \tag{3.26}$$

where $\mathbf{I}_0(z)$ is zero-order modified Bessel function of the first kind; and $\eta = \sqrt{q^2 N_a / \varepsilon_0 \varepsilon_{\mathrm{Si}} k_B T}$. Use of Eq. (3.26) in the definition of the electric displacement at the silicon-oxide interface and then of the result in Eq. (3.19) lead to

$$\sigma_c = -\varepsilon_0 \varepsilon_{\mathrm{Si}} \eta \psi_c \mathbf{I}_1(\eta R_c)/\mathbf{I}_0(\eta R_c) \tag{3.27}$$

where $\mathbf{I}_1(z)$ is first-order modified Bessel function of the first kind. We will discuss the availability of the Debye-Hückel approximation later.

Now we apply the TLM for the electrolyte-oxide interface of the SiNW. The TLM consists of the Stern layer (SL) and the diffuse layer (DL); and the SL includes the inner Helmholtz plane (IHP) and the outer Helmholtz plane (OHP) as shown in Fig. 3.8. No extra charge is in region 1 and region 2. Surface protonation reactions at the silicon oxide surface are [65]

$$> SOH + H^+ \quad = \quad > SOH_2^+ \tag{3.28a}$$

and

$$> SO^- + H^+ \quad = \quad > SOH \quad , \tag{3.28b}$$

and equilibrium reactions for adsorption of monovalent electrolyte ions with charged surface species ($> SOH_2^+$ and $> SO^-$) are

$$> SO^- + M^+ \quad = \quad > SO^-\_M^+ \tag{3.29a}$$

and

$$> SOH_2^+ + L^- \quad = \quad > SOH_2^+\_L^- \quad . \tag{3.29b}$$

where M^+ and L^- are the cation and the anion of an monovalent electrolyte, respectively. Table 3.1 shows equilibrium constants corresponding to reactions (3.28) and (3.29). The dimensionless parameters in Table 3.1 are defined by

$$\theta_+ = \frac{\nu_{>SOH_2^+}}{\Gamma_s},\ \theta_- = \frac{\nu_{>SO^-}}{\Gamma_s},\ \theta_0 = \frac{\nu_{>SOH}}{\Gamma_s},\ \theta_{+0} = \frac{\nu_{>SOH_2^+\_L^-}}{\Gamma_s},\ \text{and } \theta_{-0} = \frac{\nu_{>SO^-+M^+}}{\Gamma_s} \quad . \tag{3.30}$$

where ν_i are the equilibrium number of i species per unit area; Γ_s the total site density. The dimensionless parameters in Eq. (3.30) satisfy

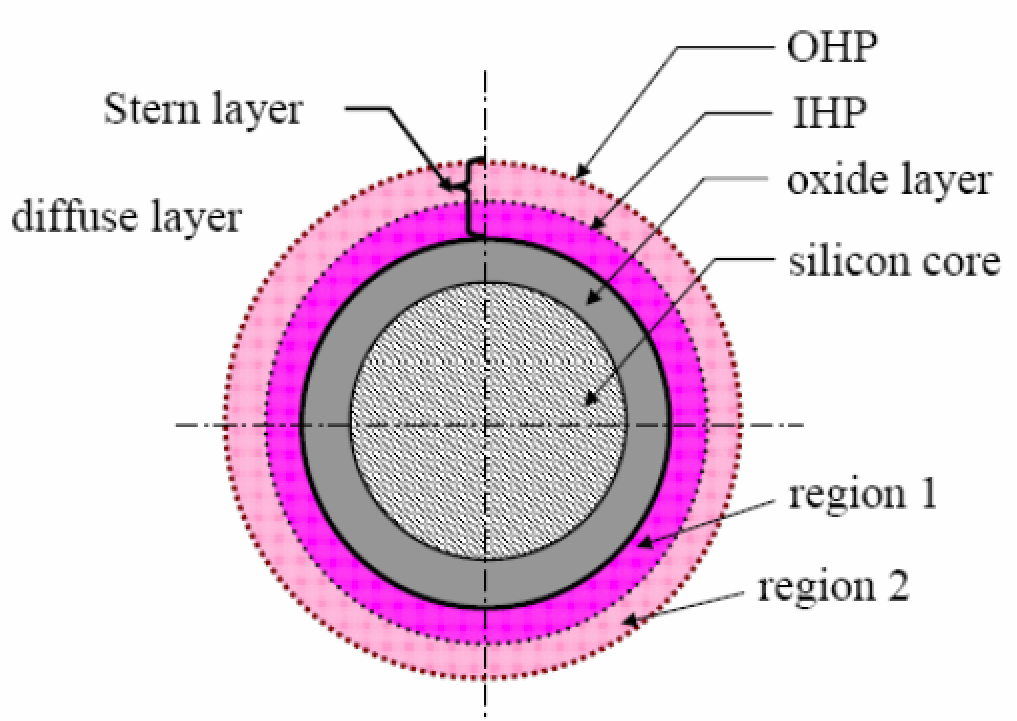

Figure 3.8. Schematic diagram of the cross section of the silicon nanowire and the electrical double layers. Stern layer includes regions 1 and 2 and the inner Helmholtz plane.

Table 3.1. Equilibrium constants corresponding to the reactions (3.28a) to (3.29b) [a].

Equilibrum reaction	Equilibrium constant	Equilibrium constant with respect to dimensionless parameters[b]
Eq. (3.28a)	$K_1 = \frac{\nu_{>SOH_2^+}}{\nu_{>SOH}\ a_{H^+}} \exp\left(\frac{q\psi_0}{k_B T}\right)$	$K_1 = \frac{\theta_+}{\theta_0\ a_{H^+}} \exp\left(\frac{q\psi_0}{k_B T}\right)$
Eq. (3.28b)	$K_2 = \frac{\nu_{>SOH}}{\nu_{>SO^-}\ a_{H^+}} \exp\left(-\frac{q\psi_0}{k_B T}\right)$	$K_2 = \frac{\theta_0}{\theta_-\ a_{H^+}} \exp\left(-\frac{q\psi_0}{k_B T}\right)$
Eq. (3.29a)	$K_{M^+} = \frac{\nu_{>SO^-\_M^+}}{\nu_{>SO^-}\ a_{M^+}} \exp\left(\frac{q\psi_\beta}{k_B T}\right)$	$K_{M^+} = \frac{\theta_{-0}}{\theta_-\ a_{M^+}} \exp\left(\frac{q\psi_\beta}{k_B T}\right)$
Eq. (3.29b)	$K_{L^-} = \frac{\nu_{>SOH_2^+\_L^-}}{\nu_{>SOH_2^+}\ a_{L^-}} \exp\left(-\frac{q\psi_\beta}{k_B T}\right)$	$K_{L^-} = \frac{\theta_{+0}}{\theta_+\ a_{L^-}} \exp\left(-\frac{q\psi_\beta}{k_B T}\right)$

[a] ψ 's represent the potential; a_i 's are regarded as dimensionless by choosing unit molarity; and the subscripts 0 and β represent the oxide surface and the IHP, respectively.

[b] The dimensionless parameters are defined by Eq. (3.30).

$$\theta_0 + \theta_{+0} + \theta_{-0} + \theta_+ + \theta_- = 1 \tag{3.31}$$

Multiplying K_1 and K_2 and using the definitions of $\mathrm{pH} \equiv -\log(a_{H^+})$ and of $\mathrm{pH}_{\mathrm{pzc}} \equiv \log(K_1 \cdot K_2)/2$, we obtain pH as

$$\mathrm{pH} = \mathrm{pH}_{\mathrm{pzc}} - \frac{1}{2.303}\frac{q\psi_0}{k_B T} - \frac{1}{2.303}\ln\left(\frac{\theta_+}{\theta_-}\right) \quad , \tag{3.32}$$

and dividing K_1 by K_2 and using Eq. (3.31) in the result yield

$$\frac{K_1}{K_2} \equiv r_K = \frac{\theta_+ \, \theta_-}{\left(1 - \alpha_+ \theta_+ - \alpha_- \theta_-\right)^2} \quad . \tag{3.33}$$

where $\alpha_+ = 1 + K_{L^-} a_{L^-} \exp\left(-q\psi_\beta / k_B T\right) = 1 + \theta_{+0}/\theta_+$ and $\alpha_- = 1 + K_{M^+} a_{M^+} \exp\left(q\psi_\beta / k_B T\right) = 1 + \theta_{-0}/\theta_-$.

Relationships among the electrostatic potentials at four interfaces—the silicon-oxide interface, the oxide surface, the IHP, and the OHP—are derived by use of Gauss' law. For simplicity, we assume that the oxide layer does not include any space charges. Thus, three layers—oxide layer, region 1 and region 2—are regarded as an insulator layer. In a coaxial cylindrical system, the electrostatic potential at the outer interface of an insulator layer is given by

$$\psi_{outside} = \psi_{inside} - Q_{inside} \ln\left(R_{outer}/R_{inner}\right)/\varepsilon_0 \, \varepsilon \tag{3.34}$$

where ψ_{inside} is the potential at the inner interface of the layer; ε the dielectric constant of the layer; R_{outer} and R_{inner} are, respectively, the outer and the inner radii of the layer; and $Q_{inside} = Q_{total}/2\pi L$; Q_{total} is the total charges inside a cylinder of the outer radius; L is the length of the cylinder. If only area charges exist inside a cylinder of the outer radius, $Q_{inside} = \sum_j R_j \, \sigma_j$ where σ_j is the charge density at an interface of radius R_j. Therefore, the relationships among the electrostatic potentials at four interfaces are as follows:

$$\psi_c = \psi_0 + \frac{R_c \, \sigma_c}{\varepsilon_0 \, \varepsilon_{ox}} \ln\left(\frac{R_0}{R_c}\right) \quad , \tag{3.35}$$

$$\psi_0 = \psi_\beta + \frac{R_c \, \sigma_c + R_0 \, \sigma_0}{\varepsilon_0 \, \varepsilon_1} \ln\left(\frac{R_\beta}{R_0}\right) \quad , \tag{3.36}$$

and

$$\psi_\beta = \psi_d + \frac{R_c \, \sigma_c + R_0 \, \sigma_0 + R_\beta \, \sigma_\beta}{\varepsilon_0 \, \varepsilon_2} \ln\left(\frac{R_d}{R_\beta}\right) \tag{3.37}$$

where ψ 's represent the electrostatic potentials; R 's are the radii; σ 's are the charge densities except σ_c; and the subscripts c, 0, β, and d represent the silicon-oxide interface, the oxide surface, the IHP, and the OHP, respectively; ε_1 and ε_2 are the dielectric constants in regions 1 and 2, respectively. The surface charge density and the charge density at the IHP are, respectively,

$$\sigma_0 = q\Gamma_s\left(\alpha_+\theta_+ - \alpha_-\theta_-\right) \quad , \tag{3.38}$$

and

$$\sigma_\beta = -q\Gamma_s\left(\theta_{+0} - \theta_{-0}\right) = -\sigma_0 + q\Gamma_s\left(\theta_+ - \theta_-\right) \quad . \tag{3.39}$$

The electrostatic potential in the DL is given by [49,50]

$$\frac{1}{r}\frac{\partial}{\partial r}\left(r\frac{\partial\psi}{\partial r}\right) = \frac{2qn_b}{\varepsilon_0\,\varepsilon_b}\sinh\left(\frac{q\psi}{k_B T}\right) \tag{3.40}$$

with boundary conditions as follows:

$$\psi(r) = \psi_d \ \text{ at } r = R_d \ \text{ and } \ \psi(r) = 0 \ \text{ at } r \to \infty \quad . \tag{3.41}$$

Here n_b is the number concentration of cations or anions in bulk sample solution, ε_b is the dielectric constant of bulk solution; R_d is the radius of the OHP. Using Debye-Hückel approximation and solving Eq. (3.40) with Eq. (3.41), we write the potential in the DL as

$$\psi(r) = \psi_d\,\mathbf{K}_0(\kappa r)/\mathbf{K}_0(\kappa R_d) \quad . \tag{3.42}$$

where $\mathbf{K}_0(z)$ is zero-order modified Bessel function of the second kind, κ is the inverse Debye length, $\kappa = \sqrt{2q^2 n_b/(\varepsilon_0\,\varepsilon_b\,k_B T)}$. By use of Eq. (3.42) in the definition of virtual charge density at the OHP $\sigma_d \equiv \varepsilon_0\,\varepsilon_b\,d\psi/dr\big|_{r=R_d}$ [49], the virtual charge density at the OHP is obtained as

$$\sigma_d = -\varepsilon_0\,\varepsilon_\mathrm{b}\,\kappa\psi_d\,\mathbf{K}_1(\kappa R_d)/\mathbf{K}_0(\kappa R_d) \tag{3.43}$$

where $\mathbf{K}_1(z)$ is first-order modified Bessel function of the second kind. Since the total charges in the SiNW and the EDL are zero, charge neutrality condition is given by

$$R_c\,\sigma_c + R_0\,\sigma_0 + R_\beta\,\sigma_\beta + R_d\,\sigma_d = 0 \tag{3.44}$$

Finally, we are ready to obtain a starting equation. Substituting ψ_c of Eq. (3.27) in Eq. (3.35) and then the result in Eq. (3.36) yield

$$R_c\,\sigma_c = -A_c\,\psi_\beta - A_c\,R_0\,\sigma_0/C_1 \tag{3.45}$$

where $A_c = \varepsilon_0 \left[\frac{\mathbf{I}_0(\eta R_c)}{\varepsilon_{\mathrm{Si}}\, \eta R_c\, \mathbf{I}_1(\eta R_c)} + \frac{1}{\varepsilon_{\mathrm{ox}}} \ln\left(\frac{R_0}{R_c}\right) + \frac{\varepsilon_0}{C_1} \right]^{-1}$ and $\frac{1}{C_1} = \frac{1}{\varepsilon_0\, \varepsilon_1} \ln\left(\frac{R_\beta}{R_0}\right)$. Replacing σ_c of Eq. (3.44) with Eq. (3.45) and then using Eqs. (3.38) and (3.39) in the result yield

$$\theta_+ = \beta\,\theta_- + \gamma \tag{3.46}$$

where $\beta = \frac{\alpha_-\left(R_0 - R_\beta - A_c\, R_0/C_1\right) + R_\beta}{\alpha_+\left(R_0 - R_\beta - A_c\, R_0/C_1\right) + R_\beta}$ and $\gamma = \frac{A_c\, \psi_\beta - R_d\, \sigma_d}{q\,\Gamma_s\, \alpha_+\left(R_0 - R_\beta - A_c\, R_0/C_1\right) + q\,\Gamma_s\, R_\beta}$. When Eq. (3.46) is used in Eq. (3.33), a quadratic equation of the dimensionless parameter θ_- is given. Thus, the dimensionless parameter θ_- is written as

$$\theta_- = \left(-b - \sqrt{b^2 - 4\,a\,c}\right)\Big/ 2\,a \tag{3.47}$$

where $a = r_K\left(\alpha_+\,\beta + \alpha_-\right)^2 - \beta$, $b = 2\,r_K\left(\alpha_+\,\beta + \alpha_-\right)\left(\alpha_+\,\beta + \alpha_-\right) - \gamma$, and $c = r_K\left(\alpha_+\,\beta + \alpha_-\right)^2$. Here, θ_- is a function of ψ_β and σ_d. Use of Eq. (3.44) in (3.37) yields

$$\psi_\beta = \psi_d - \frac{R_d\,\sigma_d}{\varepsilon_0\,\varepsilon_2} \ln\left(\frac{R_d}{R_\beta}\right) \tag{3.48}$$

Therefore, θ_- is a function of only σ_d. Eqs. (3.47) and (3.48) are starting equations to calculate every potential and charge density with the value of ψ_d or σ_d in Eq. (3.43).

Starting with the value of ψ_d or σ_d in an appropriate range, we can calculate all of the electrostatic potentials, the charge densities, and the dimensionless parameters; for example, the VCDSOI is calculated by using Eqs. (3.43), (3.48), (3.47), (3.46) and (3.46) in order. The values of the physical parameters used for the calculation are given in Table 3.2. The TLM-related parameters are determined by fitting the previous experimental result [66]. Figure 3.9 shows the pH-dependence of surface charge density at the oxide surface. The solid line is obtained by use of the TLM. The TLM is in a good agreement with the experimental result.

Figure 3.10 shows the conductance in the pH SiNW nanosensor. We used $G_0 = 800\,\mathrm{nS}$, $L = 3\,\mu\mathrm{m}$ and $R_0 = 5\,\mathrm{nm}$ for the calculation as reported in Ref. 56. To fit the conductance experimental result, the value of the dopant concentration of the SC is chosen to be 1.7×10^{25} m^{-3}. By use of G_0 in Eq. (3.21), the value of the hole mobility in the SiNW is 175.5 $\mathrm{cm}^2/\mathrm{V}\cdot\mathrm{s}$, which is in the experimental range [67]. As shown in Fig. 3.10, our model gives excellent agreement with the previous experimental conductance in the SiNW nanosensor. Since the conductance increases with increasing pH, the holes are accumulated at the silicon-oxide interface.

Table 3.2. Parameters used for the calculation.

Parameters	Values	Parameters	Values
$\log(K_2/K_1)$	7.0	$\varepsilon_{\mathrm{Si}}$	11.9
$\mathrm{pH}_{\mathrm{pzc}}$	2.8	$\varepsilon_{\mathrm{ox}}$	3.9
$\log K_{M^+}$	1.0	ε_1, ε_2 and ε_b	78
$\log K_{L^-}$	1.0	Thickness of region 1	6 Å
N_a	1.7×10^{25} m^{-3}	Thickness of region 2	6 Å
μ_p	30 ~ 560 cm^2/V s	R_c	4 nm
L	3 μm	R_0	5 nm
Γ_s	4.6×10^{18} sites/m^2	$[\mathrm{Na}^+] = [\mathrm{Cl}^+]$	0.1 M
G_0	800 nS		

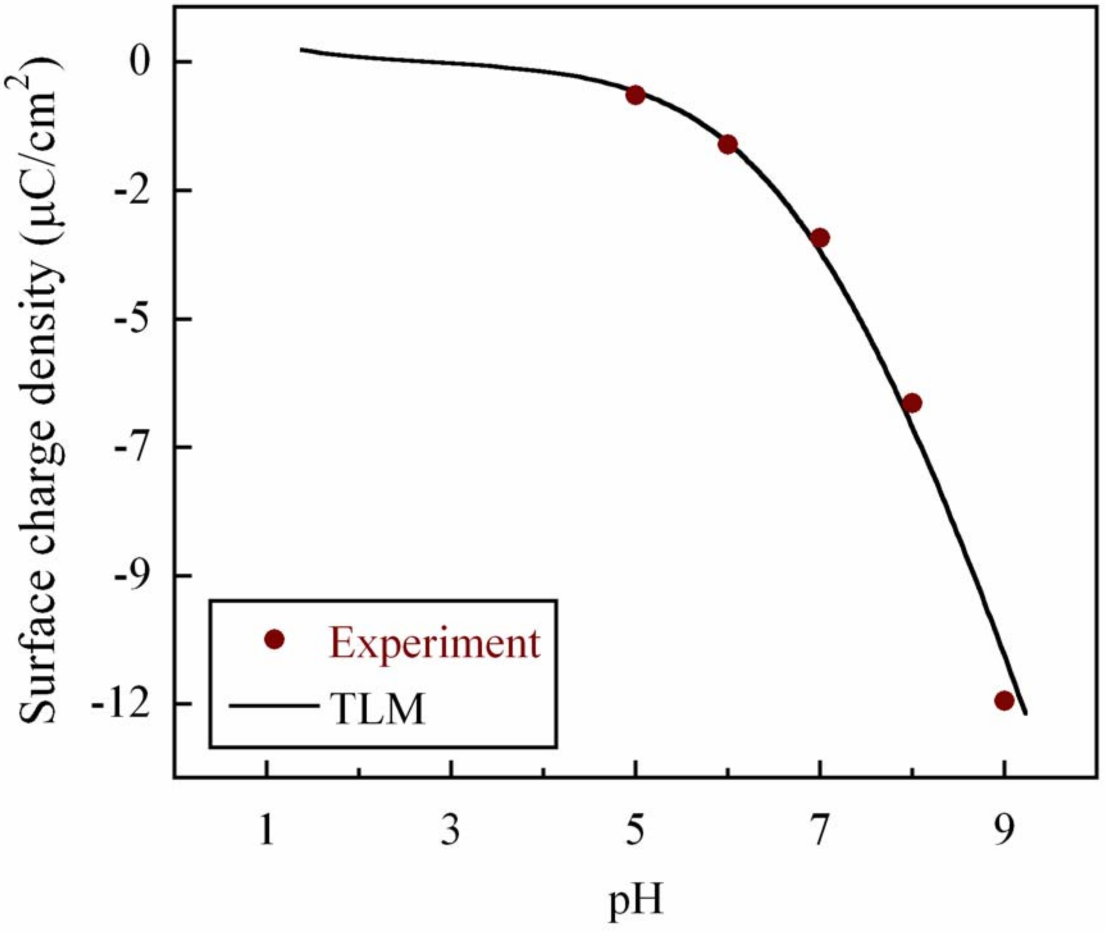

Figure 3.9. pH-dependence of the surface charge density at the oxide surface. The solid line represents the triple layer model. The circles represent the experimental result in Ref. 65.

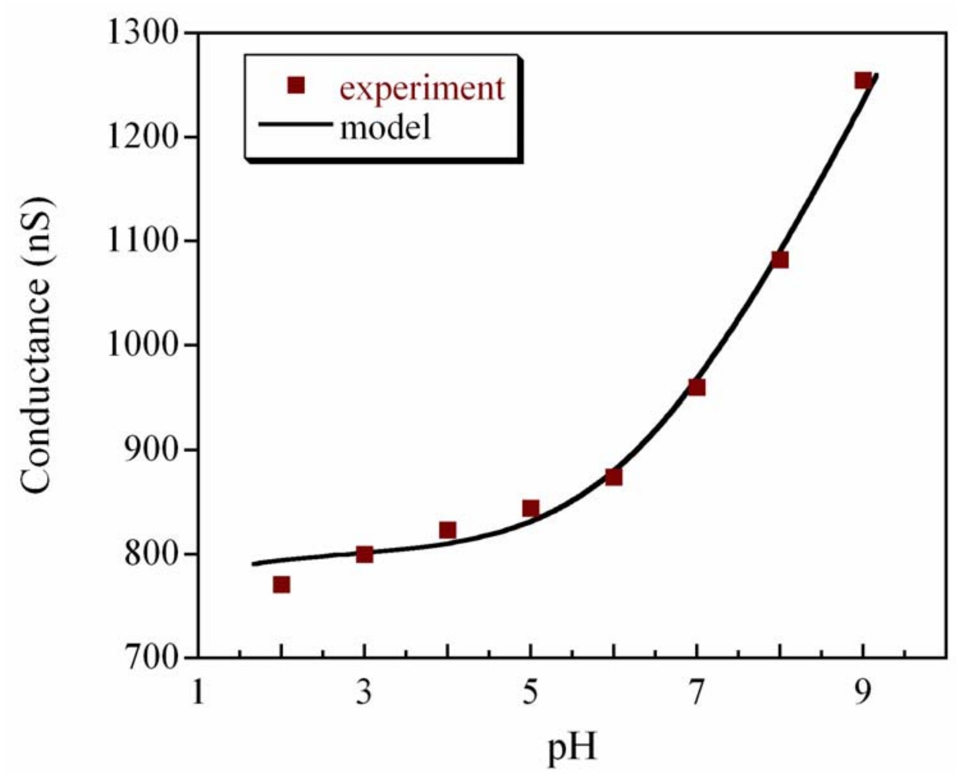

Figure 3.10. pH-dependence of the conductance in the pH silicon nanowire nanosensor. The squares represent the experimental result in Ref. 56. The values of physical parameters for the calculation are given in Table 2.

Before we discuss the sensitivity of the SiNW nanosensors, we will check whether the Debye-Hückel approximation is available in the SC and the DL. In general, the Debye-Hückel approximation gives a satisfactory result if potential is less than about 26 mV [49]. As shown in Fig. 3.11, ψ_d is always less than 20 mV but ψ_c begins bigger than 26 mV at pH of bigger than 8.3. Therefore, we can use the Debye-Hückel approximation at most of pH range.

The sensitivity of the SiNW nanosensors is defined by

$$\mathrm{S}_{\mathrm{pH}} = dG/d\mathrm{pH} = \left(2\pi\,\mu_p\,R_c/L\right)\cdot\left(d\sigma_c/d\mathrm{pH}\right) \quad . \tag{3.49}$$

The last equality is obtained by use of Eq. (3.21). As shown in Eq. (3.49), the sensitivity of the SiNW nanosensors is proportional to the hole mobility and the radius of the SC, but it is inversely proportional to the SiNW length. However, when the sensitivity is enhanced by their change, G_0 also increases, which may not be desirable. The modification of the oxide surface of the SiNW is to enhance the sensitivity; for example, the amino group at the oxide surface changes the pH-dependence of the conductance and enhances the sensitivity around the point of zero charge [4,5]. The thickness of the oxide layer affects the sensitivity; a thicker oxide layer reduces the sensitivity since the oxide layer screens the surface charges.

A new parameter, the ratio of the conductance variation to the conductance without surface effect, is introduced as follows:

$$\frac{\delta G}{G_0} = \frac{2\sigma_c}{q\,R_c\,N_a} \tag{3.50}$$

The parameter shows to what extent the surface effects can be measured with respect to G_0. If the parameter is large enough, the surface effects can be detected easily; otherwise, the surface effects cannot be distinguished from other noise. Figure 3.12 shows that the ratio increases with decreasing the radius of the SiNW. That is to say, the sensitivity of the SiNW nanosensor is enhanced more significantly at smaller radius of the SiNW.

3.2.2. *Summary*

We developed the model of the pH SiNW nanosensors. We used the triple layer model for the electrolyte-oxide interface and the diffusion-drift model for the electronic transport in the SiNW. It was shown that the conductance calculated by our model was in good agreement with the previous experimental result. Finally, we discussed the sensitivity of the SiNW nanosensors.

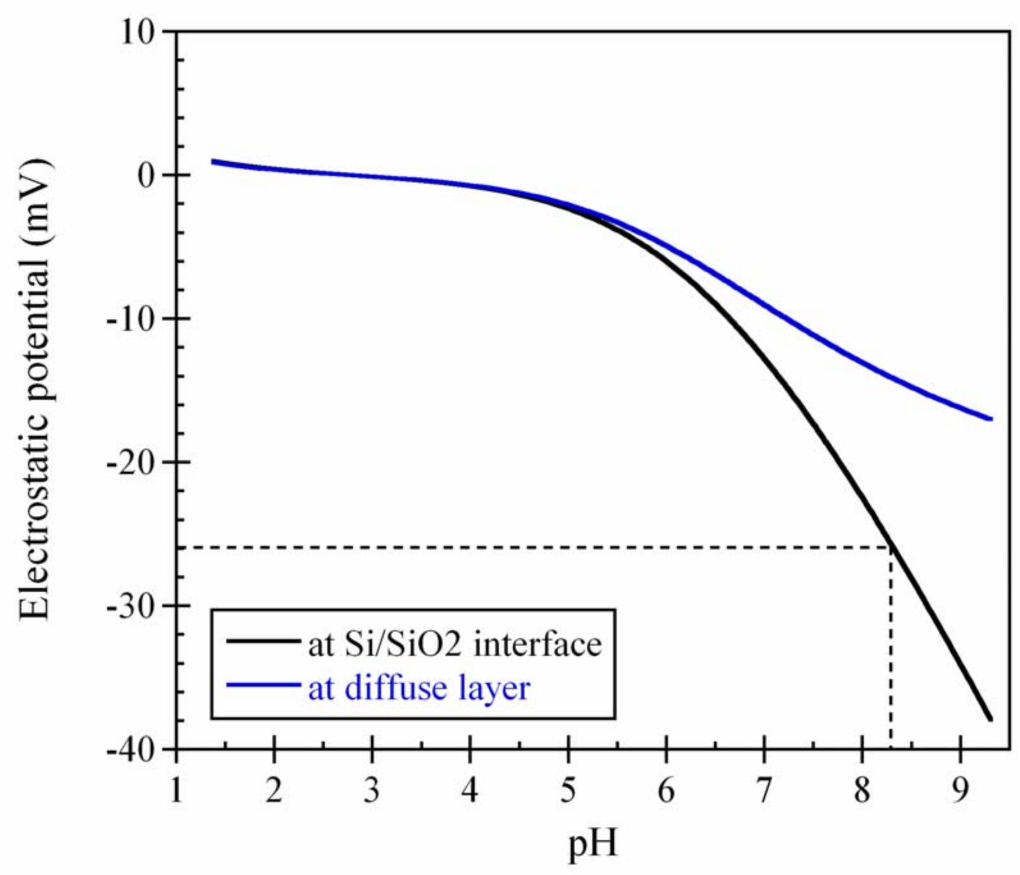

Figure 3.11. Electrostatic potentials at the silicon/silicon oxide interface and the outer Helmholtz plane.

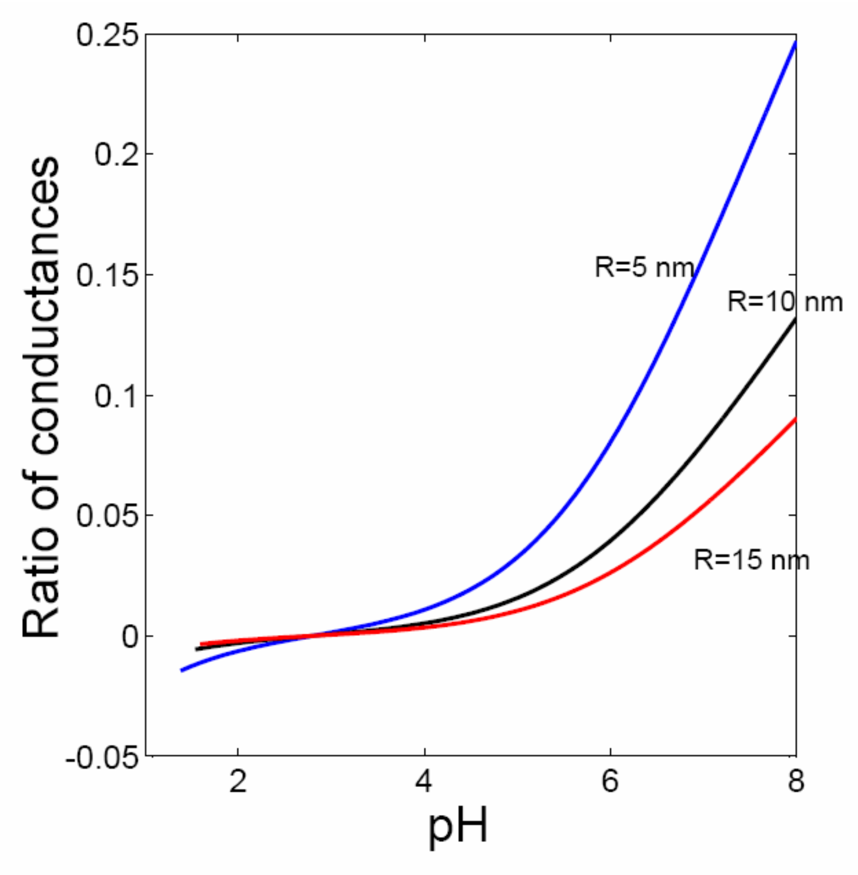

Figure 3.12. Ratio of the conductance variation to the conductance without surface effect defined by Eq. (3.50).

CHAPTER IV

SUMMARY

We discussed electronic noise in nanostructures in Chapters II and III. Chapter II deals with the manner in which the electronic noise in nanoscale digital processors can limit the operation of the processors, and Chapter III deals with how the electronic noise in nanoscale sensors can enhance the sensitivity and the selectivity of the nanosensors by using fluctuation-enhanced sensing method.

In Chapter II, we discussed the Johnson-Nyquist noise in single electron logic processors and the shot noise in current-controlled digital processors. The Johnson-Nyquist noise in single electron logic processors is regarded as thermally-assisted tunneling. We obtained the error-free performance condition. By considering the optimal operation condition, it is shown that the Johnson-Nyquist noise limits the maximal clock frequency at a given power due to dissipation. By applying the error-free performance condition, we found the maximal size of the quantum dot in the single electron transistors in order for single electron logic processors to work at room temperature. We showed that the bit-flip error rate increases very rapidly with the cutoff frequency due to the shot noise in current-controlled digital processors. By using the maximal acceptable error rate (i.e., one-bit-error per year per chip), we obtained the maximal clock frequency and the information channel capacity in current-controlled digital processors.

In Chapter III, we considered the SEnsing of Phage-Triggered Ion Cascade (SEPTIC) nanosensor and the silicon nanowire nanosensors. The SEPTIC nanosensor consists of two titanium microscale probes which are separated by nanoscale gap. We used the fluctuation-enhanced sensing method when we analyzed the signals of the SEPTIC nanosensor. We demonstrated that the SEPTIC nanosensor can detect and identify *E. coli* cells through bacteriophage infection. We discussed the origin of the fluctuations in the signals. We considered the potassium ions released from an infected cell and the electrophoretic motion of an *E. coli* cell. It was shown that the distribution of the released potassium ions becomes uniform very quickly and the ions cannot lead to the fluctuation. It was also shown that the infected cells can move faster than the normal cells since the zeta potential of the infected cell is changed. Since the cell is close to the titanium probe, we can observe more fluctuations when the cells are infected.

It is reported in the literature that the silicon nanowire nanosensors can detect a single virus and the signal from the silicon nanowire nanosensors is stochastic signal. We developed the classical model for the pH silicon nanowire nanosensors. Our model includes the triple layer model for the electrical double layer at the oxide surface/solution interface and the drift model for the electronic transport in the silicon core. The calculation results are in excellent agreement with the experimental results in the literature. It was shown that the sensitivity of the silicon nanowire nanosensor increases with decreasing the radius of the silicon nanowire.

REFERENCES

[1] G. Bastard, *Wave Mechanics Applied to Semiconductor Heterostructures*, Les Editions de Physique, Paris (1988).

[2] T. A. Fulton and G. J. Dolan, Observation of single electron charging effects in small tunnel junctions, *Physical Review Lett.* **59** (1987) 109-112.

[3] M. H. Devoret and H. Grabert, Introduction to Single Charge Tunneling, *Single Charge Tunneling*, eds. H. Grabert and M. H. Devoret, NATO ASI Ser. B Vol. 294, Plenum, New York (1992) 1-19.

[4] F. Patolsky and C. M. Lieber, Nanowire nanosensors, *Mater. Today,* **April** (2005) 20-28.

[5] C. M. Lieber, Nanscale science and technology: building a big future from small things, *MRS Bull.,* **July** (2003) 486-491.

[6] G. Chen, Z. Diao, J. U. Kim, A. Neogi, K. Urtekin, and Z. Zhang, Quantum dot computing gate, *Int. J. Quantum Inf.* **4** (2006) 233-296.

[7] Intel Press Room, Intel Introduces Intel® Pentium® 4 Processors On High-Volume 90-Nanometer Manufacturing Technology, 02/2004, http://www.intel.com/pressroom /archive/ releases/20040202comp.htm

[8] D&R Headline news**,** Process vs. density in DRAMs, 07/2005, http://www.us.design-reuse.com/news/news10806.html

[9] L. B. Kish, End of Moore's law: thermal (noise) death of integration in micro and nano electronics, *Phys. Lett. A* **305** (2002) 144-149.

[10] Yingfeng Li and L. B. Kish, Heat, speed and error limits of Moore's law at the nanoscales, *Fluct. Noise Lett.* **6** (2006) L127-L131.

[11] L.B. Kish, Noise in nanoscale electronic devices and sensors, *Defense Science Research Council Workshop on Noise and Interference in High Performance Electronics,* Arlington, TX, May 6, 2003.

[12] M. Dobozi-King, S. Seo, J.U. Kim, R. Young, M. Cheng, and L.B. Kish, Rapid Detection and Identification of Bacteria: SEnsing of Phage-Triggered Ion Cascade (SEPTIC), *J. Biol. Phys. and Chem,* **5** (2005) 3-7.

[13] F. Patolsky, G. Zheng, O. Hayden, M. Lakadamyali, X. Zhuang and C. M. Lieber, Electrical detection of single viruses, *Proc. Nat. Acad. Sci. USA*, **101** (2004) 14017-14022.

[14] Jong U. Kim, *Error rate and power dissipation in nano-logic devices*, MS thesis, Texas A&M Univ. (2004).

[15] Z. Gingl, L.B. Kiss and F. Moss, Non-dynamical Stochastic Resonance, *Europhys. Lett.,* **29** (1995) 191-196.

[16] K. K. Likharev and V. K. Semenov, Possible logic circuit based on the correlated single-electron tunneling in ultrasmall junctions, *Extended Abstracts of the International Superconductive Electronics Conference,* Tokyo, (1987) 128-131.

[17] D. V. Averin and K. K. Likharev, Possible Applications of the Single Charge Tunneling, *Single Charge Tunneling*, eds. H. Grabert and M. H. Devoret, NATO ASI Ser. B Vol. 294, Plenum, New York (1992) 324-328.

[18] D. H. Kim, S.-K. Sung, J. S. Sim, K. R. Kim, J. D. Lee, B.-G. Park, B. H. Choi, S. W. Hwang, and D. Ahn, Single-electron transistor based on a silicon-on-insulator quantum wire fabricated by a side-wall patterning method, *Appl. Phys. Lett.* **79** (2001) 3812-3814.

[19] A. N. Korotkov, Single-electron logic and memory devices, *Int. J. Electronics,* **86** (1999) 511-547.

[20] G.-L. Ingold, P. Wyrowski, and H. Grabert, Effect of the electromagnetic environment on the single electron transistor, *Zeitschrift für Physik B: Condensed Matter* **85** (1991) 443-449.

[21] S.R. Valluri, D.J. Jeffrey, and R.M. Corless, Some applications of the Lambert W function to physics, *Can. J. Phys.* **78** (2000) 823-831.

[22] J. U. Kim, L.B. Kish, Can single electronic microprocessors ever work at room temperature?, in *Proc. of SPIE* **5115** (Santa Fe, NM, USA) (2003) 174-182.

[23] D. K. Ferry and S. M. Goodnick, *Transport in Nanostructures*, Cambridge University Press, New York (1999).

[24] L.B. Kiss, Possible breakthrough: significant improvement of signal to noise ratio by stochastic resonance, *Chaotic, Fractal, and Nonlinear Signal Processing*, ed. R. Katz, AIP Press (1996) 382-398.

[25] N. G. de Bruijn, *Asymptotic methods in analysis*, 2nd Ed., North-Holland Publishing, Amsterdam (1961) 25-28.

[26] P. B. Smith, K. M. Tomfohrd, A. Balows, and D. L. Rhoden, API system: Multitube micromethod for identification of enterobacteriaceae, *Appl. Microbiol.* **24** (1972) 449-452.

[27] L. Miller, and T. Berger, Bacteria identification by gas chromatography of whole cell fatty acids, *Hewlett Packard Gas Chromatography Application Note*, Hewlett-Packard Co., Palo Alto (1985) 228-238.

[28] K. B. Mullis, and F. A. Faloona, Specific synthesis of DNA invitro via polymerase catalyzed chain reaction,. *Methods Enzymol.* **155** (1987) 355-350.

[29] L.B. Kish, R. Vajtai, C.-G. Granqvist, Extracting information from noise spectra of chemical sensors:single sensor electronic noses and tongues, *Sensors and Actuators B* **71** (2000) 55-59.

[30] G. Schmera and L. B. Kish, Surface diffusion enhanced chemical sensing by surface acoustic waves, *Sensors and Actuators B* **93** (2003) 159-163.

[31] L. B. Kish, G. Schmera, and J. Smulko, Fluctuation enhanced sensing: electronic dog nose identifies odors and counts molecules, *Nanotechnology E-Bulletin,* SPIE (2004) http://www.spie.org/paper/Sensing.pdf.

[32] R. W. Hendrix, M. C. Smith, R. N. Burns, M. E. Ford, and G. F. Hatfull, Evolutionary relationships among diverse bacteriophages and prophages: all the world's a phage, *Proc. Natl Acad. Sci.USA* **96** (1999) 2192-2197.

[33] R. B. Goldberg, R. A. Bender, S. L. Streicher, Direct selection for P1-sensitive mutants of enteric bacteria, *J. Bacteriol.* **118** (1974) 810-814.

[34] D. Kaiser and M. Dworkin, Gene transfer to myxobacterium by Escherichia coli phage P1, *Science* **187** (1975) 653-654.

[35] E. B. Goldberg, L. Grinius, and L. Letellier, Recognition, attachment and injection, *Molecular Biology of Bacteriophage T4*, eds. Karam, J. D. et al., American Society for Microbiology, Washington D.C. (1994) 347-357..

[36] L. Letellier, and P. Boulanger, Involvement of ion channels in the transport of phage DNA through the cytoplasmic membrane of E. coli, *Biochimie* **71** (1989) 167-174.

[37] J. Glenn and D. H. Duckworth, Ion fluxes during T5 bacteriophage infection of Escherichia coli, *Arch. Biochem. Biophys.* **201** (1980) 576-585.

[38] B. J. Bachmann, Pedigrees of some mutant strains of Escherichia coli K-12, *Bacteriol. Rev.* **47** (1972) 525-557.

[39] L. Randall-Hazelbauer, and M. Schwartz, Isolation of the bacteriophage lambda receptor from Escherichia coli, *J. Bacteriol.* **116** (1973) 1436-1446.

[40] V. Braun, K. Schaller, and H. Wolff, A common receptor protein for phage T5 and colicin M in the outer membrane of Escherichia coli B, *Biochim. Biophys. Acta* **323** (1973) 87-97.

[41] A. Hassibi, R. Navid, R. W. Dutton, and T. H. Lee, Comprehensive study of noise processes in electrode electrolyte interfaces, *J. Appl. Phys.* **96** (2004) 1074-1082.

[42] Ch. Kleint, Electron emission noise, *Surf. Sci.* **20**0 (1988) 472-489.

[43] C. D. Motchenbacher, J. A. Connelly, *Low-Noise ElectronicSystem Design*. New York: Wiley (1993).

[44] R. W. Hendrix, R. L. Duda, Bacteriophage lambda PaPa: not the mother of all lambda phages, *Science* **258** (1992) 1145-1148.

[45] L.B. Kish, M. Cheng, J.U. Kim, S. Seo, M.D. King, R. Young, A. Der, G. Schmera, Estimation of Detection Limits of the Phage-Invasion Based Identification of Bacteria, *Fluct. Noise Lett.* **5** (2005) L105-L108.

[46] E. S. Yang, *Fundamentals of Semiconductor Devices* (McGraw-Hill, New York, 1978).

[47] W. B. Russel, D. A. Saville, and W. R. Schowalter, *Colloidal Dispersions* (Cambridge University, Cambridge, 1989).

[48] J.R. Biard and L.B. Kish, Enhancing the sensitivity of the SEPTIC bacterium detection method by concentrating the phage-infected bacteria via DC electrical current, *Fluct. Noise Lett.* **5** (2005) L153-L158.

[49] R. J. Hunter, *Zeta Potential in Colloid Science*, Academic Press, New York (1981).

[50] R. J. Hunter, *Foundations of Colloid Science* Vol. I, Clarendon Press, Oxford (1987).

[51] D. C. Henry, The cataphoresis of suspended particles Part I - the equation of cataphoresis, *Proc. Royal Soc. Lond.* **A113** (1931) 106-129.

[52] H. Ohshima, A simple expression for Henry’s function for the retardation effect in elelctrophoresis of spherical colloidal particles, *J. Colloid Interface Sci.* **168** (1994) 269-271.

[53] A. N. Stokes, Asymptotic relations for solutions of the Poisson-Boltzmann equation for a spherical particle, *J. Chem. Phys.* **65** (1976) 261-264.

[54] J. F. Casteel and E. A. Amis, Specific conductance of concentrated solutions of magnesium salts in water-ethanol system, *J. Chem. Eng. Data* **17** (1972) 55-59.

[55] M. Tomšič, M. Bešter-Rogač, A. Jamnik, R. Neueder, and J. Barthel, Conductivity of magnesium sulfate in water from 5 to 35°C and from infinite dilution to saturation, *J. Solution Chem.* **31** (2002) 19-31.

[56] J. Hahm and C. M. Lieber, Direct ultrasensitive electrical detection of DNA and DNA sequence variations using nanowire nanosensors, *Nano Lett.* **4** (2004) 51-58.

[57] Yi Cui, Q. Wei, H. Park, C. M. Lieber, Nanowire nanosensors for highly sensitive and selective detection of biological and chemical species, *Science* **293** (2001) 1289-1292.

[58] W. U. Wang, C. Chen, K.-H. Lin, Y. Fang, and C. M. Lieber, Label-free detection of small-molecule-protein interactions by using nanowire nanosensors, *Proc. Nat. Acad. Sci. USA,***102** (2005) 3208-3212.

[59] C. D. Fung, P. W. Cheung, and W. H. Ko, A generailized theory of an electrolyte-insulator-semiconductor field effect transistor, *IEEE Trans. Electron Devices* **ED-33** (1986) 8-18.

[60] D. E. Yates, S. Levine and T. W. Healy, Site-binding model of the electrical double layer at the oxide/water interface, *J. Chem. Soc. Faraday I* **70** (1974) 1807-1818. This site-binding model is the same as the triple layer model. The inner Helmholtz plane was called β-plane.

[61] Y. Cui, X. Duan, J. Hu, and C. M. Lieber, Doping and electrical transport in silicon nanowires, *J. Phys. Chem. B* **104** (2000) 5213-5216.

[62] Y. Cui, L. J. Lauhon, M. S. Cudiksen, J. Wang, and C. M. Lieber, Diameter-controlled synthesis of single-crystal silicon nanowires, *Appl. Phys. Lett.* **78** (2001) 2214-2216.

[63] G. E. W. Bauer, Transport along doping quantum wires in silicon, *Phys. Rev. B* **43** (1991) 4023-4027.

[64] D. L. John, L. C. Castro and D. L. Pulfrey, Quantum capacitance in nanoscale device modeling, *J. Appl. Phys.* **94** (2004) 5180-5184.

[65] D. A. Sverjensky, Prediction of surface charge on oxides in salt solutions: Revisions for 1 : 1 (M+L-) electrolytes, *Geochim. Cosmochim. Acta* **69** (2005) 225-257.

[66] G. H. Bolt, Determination of the charge density of silica sols, *J. Phys. Chem.* **61** (1957) 1166-1169.

[67] Yi Cui, Z. Zhong, D. Wang, W. U. Wang and C. M. Lieber, High performance silicon nanowire field-effect transistors, *Nano Lett.* **3** (2003) 149-152.

[68] C. L. Nikias and J. M. Mendel, Signal processing with higher-order spectra, *IEEE SIGNAL PROC. MAG.* **July** (1993) 10-37.

APPENDIX
BISPECTRUM CORRELATION COEFFICIENTS

Identification and pattern recognition techniques are of crucial importance in sensing, biometric, security and image processing applications. In this appendix, we introduce a new method, which is a process recognition tool, recognizing different types of stochastic processes. The method is based on the bispectra (a higher order statistical tool) which have recently been applied to identity gases by fluctuation-enhanced gas sensing [29–31].We name this new process recognition tool bispectrum correlation coefficient (BCC) method because it utilizes normalized cross-correlation coefficients based on the bispectra of the process realizations.

Conventional cross-correlation techniques recognize only the same realization of a stochastic process, and they give zero value for the independent realizations of the same process or for two different processes. Consequently, cross-correlation techniques cannot distinguish between the case of two independent realizations of the same process and that of two different processes. In this letter, we will show that the BCC method is useful for the identification of stochastic processes even though their power density spectra (PDS) or amplitude distribution functions are indistinguishable.

The bispectrum for a stationary signal $x(k)$ is defined as [68]:

$$S_3(\omega_1,\omega_2)=\sum_{\tau_1=-\infty}^{\infty}\sum_{\tau_2=-\infty}^{\infty}E\left[x(k)x(k+\tau_1)x(k+\tau_2)\right]\cdot\exp\left[-j(\omega_1\tau_1+\omega_2\tau_2)\right] \quad , \tag{A1}$$

where τ and ω are discrete time and the angular frequency, respectively, and $E[...]$ means ensemble average. The signal is supposed to be stationary with zero mean. Due to the symmetry of the bispectrum [58], the whole information lies in the non-redundant region:

$$\omega_1 \le \omega_2, \quad 0 \le \omega_2, \quad \text{and} \quad (\tau_{i+1}-\tau_i)(\omega_1+\omega_2) \le \pi \quad . \tag{A2}$$

To calculate the bispectrum from a stationary signal of finite length, we can use the so-called direct conventional method [58]:

$$S_3(\omega_1,\omega_2)=\frac{\sum_{i=1}^{N}X_i(\omega_1)X_i(\omega_2)X_i^{*}(\omega_1+\omega_2)}{N} \quad , \tag{A3}$$

where N is the number of samples, the asterisk represents complex conjugate and $X_i(\omega)$ is the Fourier transform of the ith sample:

$$X_i(\omega)=\sum_{k=0}^{M-1} x_i(k)\exp(-jk\omega) \quad , \tag{A4}$$

where M is the length of a sample. As implied in Eq. (A.3), the bispectrum for a real-valued signal is a two-dimensional matrix with complex number elements.

To study the correlations between two bispectra, we introduce the BCC which has three different types. The "real" bispectrum correlation coefficient (RBCC) is:

$$\mathrm{RBCC}=\frac{\sum \mathrm{Re}\left[S_3^{\mathbf{i}}(\omega_1,\omega_2)\right]\cdot \mathrm{Re}\left[S_3^{\mathbf{j}}(\omega_1,\omega_2)\right]}{\sqrt{\sum\left\{\mathrm{Re}\left[S_3^{\mathbf{i}}(\omega_1,\omega_2)\right]\right\}^2\cdot\sum\left\{\mathrm{Re}\left[S_3^{\mathbf{j}}(\omega_1,\omega_2)\right]\right\}^2}} \quad , \tag{A5a}$$

the "imaginary" bispectrum correlation coefficient (IBCC) is:

$$\mathrm{IBCC}=\frac{\sum \mathrm{Im}\left[S_3^{\mathbf{i}}(\omega_1,\omega_2)\right]\cdot \mathrm{Im}\left[S_3^{\mathbf{j}}(\omega_1,\omega_2)\right]}{\sqrt{\sum\left\{\mathrm{Im}\left[S_3^{\mathbf{i}}(\omega_1,\omega_2)\right]\right\}^2\cdot\sum\left\{\mathrm{Im}\left[S_3^{\mathbf{j}}(\omega_1,\omega_2)\right]\right\}^2}} \quad , \tag{A5b}$$

and the "magnitude" bispectrum correlation coefficient (MBCC) is:

$$\mathrm{MBCC}=\frac{\sum\left\|S_3^{\mathbf{i}}(\omega_1,\omega_2)\right\|\cdot\left\|S_3^{\mathbf{j}}(\omega_1,\omega_2)\right\|}{\sqrt{\sum\left\|S_3^{\mathbf{i}}(\omega_1,\omega_2)\right\|^2\cdot\sum\left\|S_3^{\mathbf{j}}(\omega_1,\omega_2)\right\|^2}} \quad , \tag{A5c}$$

where $S_3{}^{\mathbf{i}}$ and $S_3{}^{\mathbf{j}}$ are bispectra of the i-th realization and the j-th realization. Here, Σ in Eqs. (A.5a) through (A.5c) represents the summation over the frequencies ω_1 and ω_2 in the non-redundant region. Trivially, each type of the above defined BCCs yields unity if we cross-correlate the same realization of the stochastic process with itself.

VITA

Name: Jong Un Kim

Address: Department of Electrical and Computer Engineering, Texas A&M University,
College Station, TX 77843-3128, USA

Email Address: jongkim@neo.tamu.edu

Education:

Ph.D.,	Electrical Engineering,	Texas A&M University,	2006
M.S.,	Electrical Engineering,	Texas A&M University,	2004
Ph.D.,	Chemical Engineering,	Seoul National University,	2000
M.S.,	Chemical Engineering,	Seoul National University,	1995
B.S.,	Chemical Engineering,	Seoul National University,	1993

Research interests:

Electronic structure and transport in nanostructures
Application of nanostructures in sensing

Publications:

1. J. U. Kim, *Model for the motility of flagellated bacteria,* Submitted for publication.
2. J. U. Kim, *Modeling pH silicon nanowire nanosensors,* Submitted for publication.
3. J. U. Kim and L. B. Kish, *Recognizing different types of stochastic processes, Fluct. Noise Lett.* **6** (2006) L1-L5.
4. G. Chen, Z. Diao, J. U. Kim, A. Neogi, K. Urtekin, and Z. Zhang, *Quantum dot computing gates, Int. J. Quantum Inf.* **4** (2006) 233-296.
5. M. D. King, S. Seo, J. U. Kim, R. Young, M. Cheng, and L. B. Kish, *Rapid detection and identification of bacteria: Sensing of phage-triggered ion cascade, J. Biol. Phys. and Chem.* **5** (2005) 3-7.
6. L. B. Kish, M. Cheng, J. U. Kim, S. Seo, M. D. King and R. Young, *Estimation of detection limits of the phage-invasion based identification of bacteria, Fluct. Noise Lett.* **5** (2005) L105-L158.
7. J. U. Kim and L. B. Kish, *Error rate in current-controlled logic processors with shot noise, Fluct. Noise Lett.* **4** (2004) L83-L86.
8. J. U. Kim and L. B. Kish, *Can single electron logic microprocessors work at room temperature?, Phys. Lett. A* **323** (2004) 16-21.